Schweizerische Eidgenossenschaft
Confédération suisse
Confederazione Svizzera
Confederaziun svizra

Eidgenössisches Departement für
Umwelt, Verkehr, Energie und Kommunikation UVEK

Office fédéral de l'énergie OFEN

STOCKAGE DE FROID PAR FLUIDE DIPHASIQUE POUR TRANSPORT ET DISTRIBUTION DU FROID, POUR LA CLIMATISATION ET/OU PROCESSUS INDUSTRIELS

ÉTUDE DE FAISABILITÉ II

Rapport final

Auteur et coauteurs	Jin HU, Osmann SARI, Frederic BRUN, Sarah EICHER
Institution mandatée	HEIG-VD- Institut de Genie Thermique, Axima Refrigeration, Nestlé
Adresse	Avenue des Sports 14, 1400 Yverdon-les-Bains
Téléphone, e-mail, site Internet	079 647 21 30,osmann.sari@heig-vd.ch
N° projet / n° contrat OFEN	101585
Responsable OFEN du projet	Osmann SARI
Durée prévue du projet (de - à)	
Date	1er février 2008

RÉSUMÉ

In the present report, 2 large-scale continuous CO_2 hydrate formation-dissociation conditions were experimentally investigated on a fully functional laboratory demonstrator for industrial applications.

The solid fraction of CO_2 hydrate slurry was evaluated by a numerical approach based on a CO_2 mass balance.

A first CO_2 hydrate slurry production system with compressor was tested. In this system the CO_2 hydrate slurry formation and dissociation pressure, temperature, density and dynamic viscosity were measured. The consumption of CO_2 hydrate slurry in the consumer installed in the climate room was successful;. The continuous formation and dissociation processes in this loop were not very successful.

A second experimental loop for hydrate production without compressor was completed. The new test rig is an industrial prototype approach. The new test rig is simple, easy to be modified and adapted to new devices. Axima heat exchanger was modified and is being used for hydrate slurry production. Kenics mixing elements and Sulzer SMV gas mixers were tested in the loop. Experimental results showed that the mixing elements and gas mixers can promote hydrate formation.

CO_2 hydrate slurry density was measured with a value of 1032 kg/m^3 which corresponds to over 30% solid fraction (150 kJ/kg dissociation enthalpy of water). Power of the pump was tested and it was showed that it is not sufficient to pump CO_2 hydrate slurry when density is over 1030 kg/m^3;

The Cp of water and of ice, the enthalpy of ice and of CO_2 hydrates were obtained using a differential scanning calorimetry, Micro DSCVII. It confirmed that CO_2 dissolved in water depresses the freezing point of water.

On-line measurements of corrosion rates were performed and reliable results obtained.

Table of Contents

Nomenclature 3
1. Introduction 5
2. Objectives 7
3. The Numerical Approach 8
  3.1 Determination of Hydrate Solid Fraction 8
4. The Experimental Approach 16
  4.1 CO_2 Hydrate Slurry Production System with Compressor 16
  4.2 CO_2 Hydrate Slurry Production System without Compressor 18
    4.2.1 CO_2 Hydrate Slurry Production Unit: Axima Heat Exchanger 20
  4.3 Measurement Techniques 21
    4.3.1 Measurement of Temperature 21
    4.3.2 Measurement of Mass Flow Rate 22
    4.3.3 Measurement of the Fluid Density 22
    4.3.4 Measurement of the Heat Capacity and Enthalpy 22
    4.3.5 Measurement of Dynamic Viscosity of CO_2 Solution and CO_2 Hydrate Slurry 25
    4.3.6 Measurement of Corrosion Rate of CO_2 Solution and CO_2 Hydrate Slurry on Different Materials 26
5. Experimental Results 27
  5.1 Experimental Results of CO_2 Hydrate Slurry Production System with Compressor 27
    5.1.1Temperature and Pressure Profiles of CO_2 Hydrate Slurry Formation and Dissociation 27
    5.1.2 Density of CO_2 Solution and CO_2 Hydrate Slurry 28
    5.1.3 Dynamic Viscosity of CO_2 Solution and CO_2 Hydrate Slurry 29
  5.2 Tap Water Test in the New Test Rig without Compressor 29
    5.2.1 Temperature Profiles of the Fluid 29
    5.2.2 Mass Flow Rate of Different Fluids in Different Loops 32
    5.2.3 Energy Balance for Heat Exchangers and Chillers 32
    5.2.4 Density Measurement 34
  5.3 Continuous CO_2 Hydrate Slurry Production in the New Test Rig without Compressor 35
    5.3.1 Temperature and Power Profiles in the Loops 35
    5.3.2 Mass Flow Rate of Different Fluids 37
    5.3.3 Pressure in the Loop 37
    5.3.4 Water and CO_2 Solution Preliminary Density Measurements 38
    5.3.5 CO_2 Solution and CO_2 Hydrate Density 39
  5.4 Micro DSCVII Results 39
    5.4.1 Heat Capacity of Water 39
    5.4.2 The Dissociation Enthalpy of Ice 40
    5.4.4 Determination of Freezing Point of Water in Micro DSCVII 41
    5.4.5 Determination of Freezing Point of Water with Dissolved CO_2 in Micro DSCVII... 42
    5.4.6 Measurements of CO_2 Hydrate-Ice Mixture 43
  5.5 Corrosion Measurement 45
6. Conclusions 49
7. Future Work 51
  7.1 Optimization of CO_2 Hydrate Slurry Production Loop 51
  7.2 Determination of Flow Properties of CO_2 Hydrate Slurry 51
    7.2.1 Aims of the Viscosity Measurements 52
  7.3 Development of CFD Models to Simulate CO_2 Hydrates Formation/Re-formation Process inside Heat Exchanger 52
References 55

Nomenclature

n	Hydration number 5.75≤ n ≤7.67 n=6.2 for all the calculations	
X	The numbers of the occupied small cavities x (≤ 2)	
Y	The numbers of the occupied large cavities y (≤ 6)	
$n_{CO_2,free}$	The total mole of CO_2 at Free State	
$n_{CO2,total}$	The total mole of CO_2 gas injected in the hydrate formation reactor	
$n_{CO2,hydrate}$	The total mole of CO_2 in the form of CO_2 hydrate	
$n_{CO_2,water}$	The total mole amount of CO_2 dissolved in the water	
R	Universal gas constant	R= 8.314 J/ K· mol
T	Temperature	K, °C
V	Volume	m^3
P	Pressure	bar
V_{total}	The total volume of the hydrate formation reactor	
V_{liquid}	The total volume of liquid phase	
$V_{hydrate}$	The total volume of hydrate	
ρ_{liquid}	The density of CO_2 solution	
M_{H_2O}	Mole mass of water, in g/mol	(M_{H_2O}=18.015257 g/mole)
M_{CO_2}	Mole mass of CO_2,	n g/mol
$n_{H_2O,total}$	The total mole amount of water in the hydrate formation reactor	
$n_{H_2O,hydrate}$	The total mole amount water in the form of CO_2 hydrate	
$n_{hydrate}$	The total mole amount of hydrate formed in the reactor	
ρ_{H_2O}	Pure water density	kg/m^3
V_w	Molar volumes of pure water V_w	
m_{CO_2}	Solubility of CO_2 gas in the water under critical pressure and temperature	
y_{CO_2}	The mole fraction of CO_2 in vapour phase	
ϕ_{CO_2}	The fugacity coefficient of CO_2	
$\mu^{l(0)}_{CO_2}$	The standard chemical potential of CO_2 in liquid phase	
λ_{CO_2-Na}	The interaction parameter between CO_2 and Na^+, Cl^-	
P_{H2O}	The pure water pressure, which can be taken from the steam tables	
Tc	The critical temperature of water	Tc = 647.29 K
Pc	The critical pressure of water	Pc = 220.85 bar

v_w^β	Mole volume of CO_2 hydrate
N_A	Avogardro’s number
N_w^β	The number of water molecules per hydrate cell
$V_{hydrate}$	The total volume of solid CO_2 hydrates occupied

1. Introduction

Les dangers de l'impact des fluides frigorigènes synthétiques sur l'environnement ainsi que les importantes mesures de sécurité, poussent l'industrie du froid à rechercher et à s'engager sur de nouvelles voies permettant de supprimer certains gaz ou d'en diminuer les quantités dans les installations. Une des solutions est l'utilisation du "coulis dyphasique " comme fluide caloporteur (technologie du refroidissement indirect).

La formation des hydrates, Clathrate - hydrate est assez récente et date des années 1930. La combinaison entre de l'eau et du CO_2 sous forme gazeuse et sous certaines conditions de température, pression, permet d'obtenir des hydrates. Le processus de formation des hydrates ($CO_2.nH_2O$) est décrit selon :

$$CO_2 + nH_2O \leftrightarrow CO_2.nH_2O$$

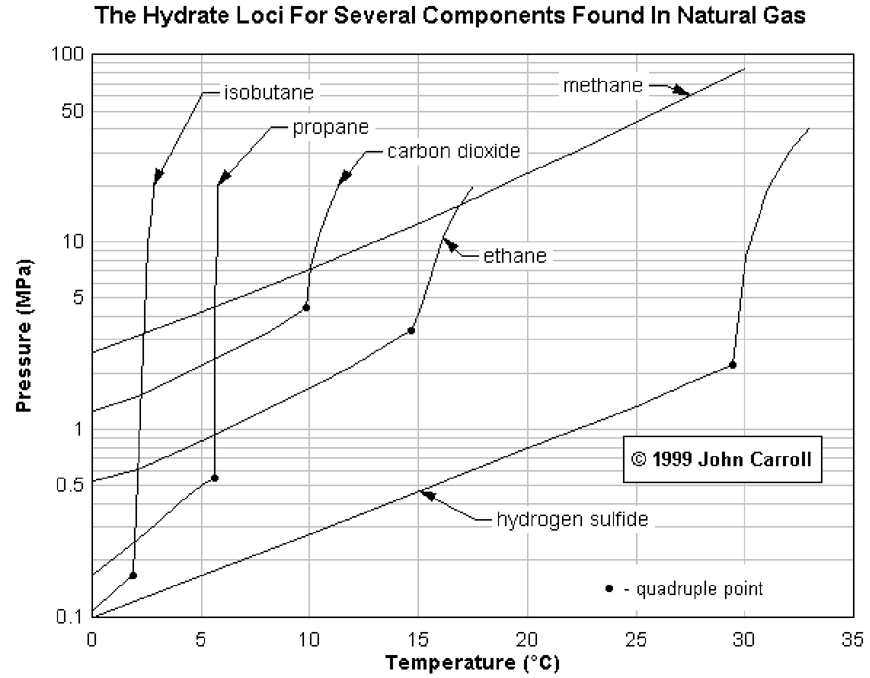

Figure 1.1 Diagramme des Hydrates

A ce jour et à notre connaissance, les travaux publiés ont été réalisés à l'échelle microscopique par Marinhas *et al.* (2006).

Pour le moment aucune expérience de taille utile n'a été réalisée dans le monde scientifique. Cependant il faut imaginer que tout n'est pas publié, notamment au Japon, surtout s'il y a des débouchés commerciaux comme c'est le cas**.**

C'est dans le cadre des activités internes du laboratoire de Thermique Industrielles et Systèmes (TiS) de l'Institut de Génie thermique (IGT) de la Haute Ecole d'Ingénierie et de Gestion du Canton de Vaud (HEIG-VD) qu'un premier démonstrateur statique a été conçu et construit.

Le principe de la production d'hydrates repose sur l'injection directe de CO_2 gazeux dans de l'eau. Un banc d'essai a été conçu et construit pour une pression de service de 40 bar pour produire des coulis d'hydrates par injection de CO_2 sous forme gazeuse dans de l'eau contenue dans un cylindre de 1200 mm de long et 150 mm de diamètre.

Les premiers essais « statiques » ont permis de visualiser la production d'hydrates de CO_2 dans de l'eau à 3 °C et sous une pression de 25 bar.

La production de coulis d'hydrates de CO_2 est validée. Il est dès lors important de poursuivre ces travaux sur une production – en continu et sur une boucle - du coulis d'hydrates de CO_2 à l'échelle de laboratoire et en grande quantité.

Le banc d'essai initial a été modifié afin de créer une boucle de circulation en continu du CO_2. Un compresseur et un refroidisseur du CO_2 ont été implantés sur le circuit initial.

2. Objectives

Le but de ce projet en partenariat avec AXIMA REFRIGERATION comme partenaire industriel principal et Nestlé SA comme utilisateur final est :

- Valider la faisabilité d'une distribution et utilisation - en continu - de coulis d'hydrates de CO_2 dans une chambre climatique de laboratoire de 4 x 4 x 3 mètres;
- Estimer les performances énergétiques de ce système et en étudiant l'impact que pourraient avoir de tels équipements sur la consommation d'énergie;
- Analyser les contraintes et les difficultés techniques, particulièrement en terme d'industrialisation, imposée par la réalisation de tels systèmes;
- Notre participation à l'annexe 20 de l'IEA.

3. The Numerical Approach

3.1 Determination of Hydrate Solid Fraction

CO_2 hydrate slurry is obtained by simply injecting CO_2 gas in a cooled liquid under certain conditions of temperature and pressure. The process of hydrate formation is described by the formula (3.1).

$$CO_2 + nH_2O \leftrightarrow CO_2 \cdot nH_2O \tag{3.1}$$

The chemical formula for CO_2 hydrate is $(x + y)\ CO_2{\cdot}46H_2O$, where x (≤ 2) and y (≤ 6) represent the numbers of the occupied small and large cavities, respectively. Each cavity can hold at most one CO_2 molecule. If all of the cavities are occupied, then $x + y = 8$, leading to the common expression of $8CO_2{\cdot}46H_2O$ or $CO_2{\cdot}\ 5.75H_2O$ for CO_2 hydrate.

Predicting cage occupancies and hydration number (the average number of water molecules per guest molecule in the hydrate) of the hydrate phase is important for evaluating the amount of gas stored in the hydrate phase. However, the practical expression for CO_2 hydrate could be $6CO_2{\cdot}46H_2O$ or $CO_2{\cdot}7.67H_2O$, i.e. CO_2 hydrate is a non-stoichiometric compound. Thus, the hydration number *n* is in the range: $5.75 \leq n \leq 7.67$.

However, since gas hydrates are non-stoichiometric compounds, stability of the structure can only be obtained with an occupation rate lower than 100%. This means that, in the case of CO_2 hydrate, n is higher than the stoichiometric value of 5.75. Therefore, in this investigation, the hydrate number n for CO_2 hydrate will be taken equal to 6.2 in accordance to Rui Sun et al. (2005).

In a CO_2 hydrate slurry production system, CO_2 always exists in three forms:

- free gas, under certain pressure and temperature conditions and obeying the ideal gas law;
- dissolved in the solution and not converted into hydrates (depends on pressure, temperature and solubility of the solution),
- clathrate hydrate.

The CO_2 mass balance involves equalising the total amount of CO_2 before and after hydrate crystallisation. This model is based on a CO_2 mass balance at hydrate-liquid-vapour (HLV) equilibrium. The total amount of CO_2 in the system is, then taken as a source term. The amount of free CO_2 gas is expressed as:

$$n_{CO_2,free} = \left(\frac{P_{CO_2}}{RT}\right) \cdot \left(V_{total} - V_{liquid} - V_{hydrate}\right) \tag{3.2}$$

where R is the Universal gas constant taken as 8.314 J/ K· mol, T is the temperature in K; V is the volume in m^3; P is the pressure in pascal; $n_{CO_2,\ free}$ is the total mole amount of CO_2 in free state; V_{total} is the total volume of the reactor for hydrate formation; V_{liquid} is the apparent total volume of liquid phase and $V_{hydrate}$ is the total volume of hydrate.

With:

$$V_{liquid} = \frac{\left(n_{H_2O,total} - n_{H_2O,hydrate}\right)}{\rho_{liquid}} \cdot M_{H_2O} \tag{3.3}$$

where ρ_{liquid} is the density of CO_2 solution; M_{H_2O} is mole mass of water in g/mol; $n_{H_2O,\ total}$ is the total mole amount of water in the reactor; $n_{H_2O,\ hydrate}$ is the total mole amount of water in the form of hydrate.

The mole volume of pure water

The mole volume of pure water V_w proposed by Jiawen Hu *et al.* (2007) is:

$$V_w = k_0 + k_1 P + k_2 P^2 + k_3 P^3 \tag{3.4}$$

$$k_0 = k_{01} T^3 + k_{02} T^2 + k_{03} T + k_{04} + \frac{k_{05}}{T} \tag{3.5}$$

$$k_1 = k_{11} T^3 + k_{12} T^2 + k_{13} T + k_{14} + \frac{k_{15}}{T} \tag{3.6}$$

$$k_2 = k_{21} T^3 + k_{22} T^2 + k_{23} \tag{3.7}$$

$$k_3 = k_{31} T^3 + k_{32} T^2 + k_{33} \tag{3.8}$$

Table 3.1 Constants in Equations (3.4) to (3.8)

k_{01}	3.27225E-07	k_{14}	3.59860E-02
k_{02}	-4.20950E-04	k_{15}	-3.55071
k_{03}	2.32594E-01	k_{21}	2.57241E-14
k_{04}	-4.16920E+01	k_{22}	-1.24336E-11
k_{05}	5.71292E+03	k_{23}	5.42707E-07
k_{11}	-2.32306E-10	k_{31}	-4.42028E-18
k_{12}	2.91138E-07	k_{32}	2.10007E-15
k_{13}	-1.49662E-04	k_{33}	-8.11491E-11

The density of pure water

Theoretical values for the density of water were taken from Jiawen Hu *et al*. (2007) using equations (3.3) to (3.9).

$$\rho_{H_2O} = \frac{M_{H_2O}}{V_w} \tag{3.9}$$

with M_{H_2O} equal to 18.015257 g/mole and V_w, T and P units in cm^3/mol, K and bar, respectively. This equation reproduces the water volumes of Wagner and Pruss (2002) with an average deviation of 0.005% and a maximum deviation of 0.027% in the range 273.15 – 473.15 K and 0 – 200 MPa.

The density of the CO_2 solution

$$CO_2\ \text{Mole} = \frac{\text{Total}\ CO_2\ \text{Mass}}{M_{CO_2}} \tag{3.10}$$

where $M_{\mathrm{CO_2}}$ is mole mass of CO_2 in g/mol;

$$\mathrm{H_2O\ Mole} = \frac{\mathrm{Total\ Water\ Mass}}{\mathrm{M_{H_2O}}} \tag{3.11}$$

$$\mathrm{y(2)} = \frac{\mathrm{CO_2Mole}}{\mathrm{CO_2Mole + H_2OMole}} \quad \text{in mol/mol} \tag{3.12}$$

$$\mathrm{y\ (1) = 1 - y(2)} \tag{3.13}$$

$$\mathrm{C} = \mathrm{T}^2 \times (\mathrm{a}_1 + \frac{\mathrm{a}_2}{\mathrm{T}} + \frac{\mathrm{a}_3}{\mathrm{T}^2} + \frac{\mathrm{a}_4}{\mathrm{T}^3} + \frac{\mathrm{a}_5}{\mathrm{T}^4}) \tag{3.14}$$

$$\mathrm{d} = \mathrm{T}^2 \times (\mathrm{a}_6 + \frac{\mathrm{a}_7}{\mathrm{T}} + \frac{\mathrm{a}_8}{\mathrm{T}^2} + \frac{\mathrm{a}_9}{\mathrm{T}^3} + \frac{\mathrm{a}_{10}}{\mathrm{T}^4}) \tag{3.15}$$

Table 3.2 Constants in Equations (14) and (15)

a_1	0.0003838402
a_2	-0.5595385
a_3	304.29268
a_4	-72044.305
a_5	6300338.8
a_6	-0.00000057709332
a_7	0.00082764653
a_8	-0.43813556
a_9	101.44907
a_{10}	-8677.7045

$$\mathrm{V_{liquid}} = \mathrm{Vw} + [1 + (\mathrm{c} + \mathrm{d}\ \ \mathrm{P})\ \ \mathrm{y(2)}] \tag{3.16}$$

$$\rho_{\mathrm{liquid}} = \frac{\mathrm{y(1) * H_2OMoleMass + y(2) * CO_2MoleMass}}{\mathrm{V_{liquid}}} * 1000000 \quad \text{in g/m}^3 \tag{3.17}$$

with T and P in K and bar, respectively.

Theoretical values for the density of the CO_2 solution were taken from Jiawen Hu *et al.* (2007) and Duan, Z. *et al.* (2003, 2006)using equations (3.10) to (3.17).

Based on the chemical equation (3.1), we can deduct at the HLV equilibrium:

$$\frac{1}{n} n_{H_2O,\mathrm{liquid}} = n_{\mathrm{hydrate}} = n_{CO_2,\mathrm{hydrate}} \tag{3.18}$$

where *n* equals 6.2 and $n_{hydrate}$ is the total mole amount of hydrate formed.

The dissolved CO_2 in the water can be expressed as:

$$n_{CO_2,\mathrm{water}} = m_{CO_2}\left(n_{H_2O,\mathrm{total}} - n_{H_2O,\mathrm{hydrate}}\right) \tag{3.19}$$

where $n_{CO_2,water}$ is the mole amount of CO_2 dissolved in the water and m_{CO_2} is the solubility of CO_2 gas in the water under critical pressure and temperature.

CO_2 solubility in the water

Over the past decades there have been many experimental studies on the CO_2-H_2O and CO_2-H_2O-salt systems, over a wide pressure-temperature range. At the same time theoretical efforts have been made to model the solubility of carbon dioxide in aqueous solutions (Nighswander *et al.* (1989); Carroll *et al.* (1991); King *et al.* (1992); Larryn W. Diamond *et al.* (2003); Duan and Sun (2003); Duan *et al.* (2006); Portier and Rochelle (2005). The most complete model developed until now is that of Duan and Sun (2003, 2006), which models the solubility of CO_2 in pure water and aqueous solutions from 0 to 260 °C and from 0 to 2000 bar total pressure, up to ionic strengths of 4.5 mol/kg water. The model is extended not only to predict the solubility of CO_2 in pure water and NaCl solution but also in more complex systems, which may include Ca^{2+}, K^{+}, Mg^{2+}, and SO_4^{2-} ions.

On the basis of the Equation of State (EOS) developed by Duan *et al.* (1992a, 2006), Duan and Sun (2003, 2006), derived a theoretical model for calculating the solubility of CO_2 in pure water and aqueous NaCl solutions. They used the EOS of Duan *et al.* (1992a, 2006) to represent the chemical potential of carbon dioxide in the vapour phase; the interaction model of Pitzer (1973) describes the chemical potential in the liquid phase. As already indicated, the model is valid for temperatures from 0 to 260 °C and pressures from 0 to 2000 bars. Although Duan's model is developed for calculating the solubility in NaCl solutions up to an ionic strength of 4.5 M, the model is also extended to calculate the solubility of carbon dioxide in more complex solutions containing K^{+}, Mg^{2+}, Ca^{2+}, and SO_4^{2-}.

The final form of Duan's solubility model is:

$$\begin{aligned}\ln m_{CO_2} &= \ln\left(y_{CO_2}\right)\cdot\phi_{CO_2}\cdot P - \frac{\mu^{l(0)}_{CO_2}}{RT} - 2\lambda_{CO_2-Na}\cdot(m_{Na}+m_K+2m_{Ca}+2m_{Mg})\\ &-\xi_{CO_2-Na-Cl}\cdot m_{Cl}\cdot(m_{Na}+m_K+m_{Ca}+m_{Mg})+0.07m_{SO_4}\end{aligned} \tag{3.20}$$

where T is absolute temperature in Kelvin, P is the total pressure of the system in bar, R is universal gas constant, m means the molality of components dissolved in water, y_{CO2} is the mole fraction of CO_2 in vapour phase, ϕ_{CO_2} is the fugacity coefficient of CO2, $\mu_{CO_2}^{l(0)}$ is the standard chemical potential of CO2 in liquid phase, λ_{CO_2-Na} is the interaction parameter between CO2 and Na$^+$, $\xi_{CO_2-Na-Cl}$ is the interaction parameter between CO2 and Na$^+$, Cl$^-$. All parameters presented in Equation (3.20) can be calculated directly without any iteration, except the fugacity coefficient of CO2, ϕ_{CO_2}, which is calculated from the fifth order virial EOS developed by Duan *et al.* (1992), and a time-consuming iterative procedure was needed to solve the EOS.

For water-CO2 system, CO2 solubility in the water can be simplified to the following equation:

$$\ln\left(m_{CO_2}\right) = \ln\left(y_{CO_2}\right) \cdot \phi_{CO_2} \cdot P - \frac{\mu_{CO_2}^{l(0)}}{RT} \tag{3.21}$$

$$y_{CO_2} = \frac{P - P_{H_2O}}{P} \tag{3.22}$$

where P_{H_2O} is the pure water pressure, which can be taken from the steam tables (Haar *et al.* (1984)) or can be calculated from an empirical equation; ϕ_{CO_2} can be calculated by a non-iterative equation as a function of temperature and pressure (Equation 3.24); $\frac{\mu_{CO_2}^{l(0)}}{RT}$ is dependent upon temperature and total pressure (Equation 25);

The empirical model to calculate pure water pressure has the following form:

$$P_{H_2O} = (\frac{P_C T}{T_C})[1 + c_1(-t)^{1.9} + c_2 t + c_3 t^2 + c_4 t^3 + c_5 t^4] \tag{3.23}$$

where T is temperature in K, $t = \frac{T - Tc}{Tc}$. T_c and P_c are the critical temperature and critical pressure of water, respectively (T_c = 647.29 K, P_c = 220.85 bar). The parameters of Equation (3.23) are listed in Table 3.3.

Table 3.3 Constants in Equation (3.23)

c₁	-38.640844
c₂	5.8948420
c₃	59.876516
c₄	26.654627
c₅	10.637097

$$\phi_{CO_2} = c_1 + P.[c_2 + c_3 T + \frac{c_4}{T} + \frac{c_5}{T-150}] + P^2 \cdot [c_6 + c_7 T + \frac{c_8}{T}] + \ln P.[c_9 + c_{10} T + \frac{c_{11}}{T}] + \frac{c_{12} + c_{13} T}{P} + \frac{c_{14}}{T} + c_{15} T^2 \tag{3.24}$$

for which:

P_1 = saturation pressure of CO_2	273 K < T <573 K
P_1=75 + (T-305)×1.25	305 K < T <405 K
P_1=200 bar	T > 405 K
P_1<P<1000 bar	273 K < T<340 K
P >1000 bar	273 K < T <340 K
P_1<P<1000 bar	340 K < T <435 K
P >1000 bar	340 K<T<435 K
P >P_1	T >435 K

Following Pitzer *et al.* (1984), the following equation for the parameters $\frac{\mu^{l(0)}_{CO_2}}{RT}$ was selected:

$$\frac{\mu^{l(0)}_{CO_2}}{RT} = c_1 + c_2 T + \frac{c_3}{T} + \frac{c_4}{T^2} + \frac{c_5}{630 - T} + c_6 P + c_7 P \ln T + \frac{c_8 P}{T} + \\ + \frac{c_9 P}{630 - T} + \frac{c_{10} P^2}{(630 - T)^2} + c_{11} T \ln P \qquad (3.25)$$

Table 3.4 T-P Range to Calculate Fugacity Coefficient of CO_2, ϕ_{CO_2}

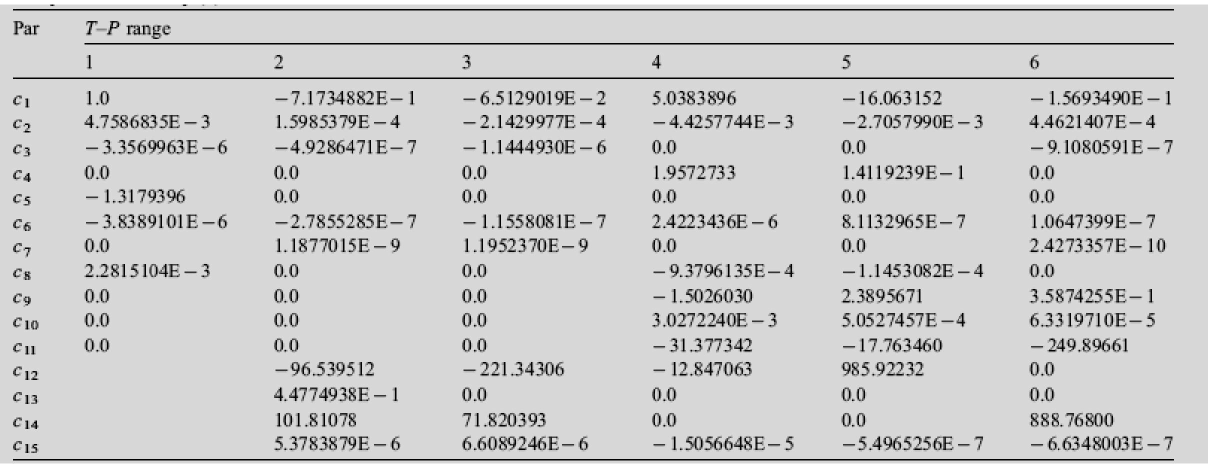

Par	T–P range					
	1	2	3	4	5	6
c_1	1.0	−7.1734882E−1	−6.5129019E−2	5.0383896	−16.063152	−1.5693490E−1
c_2	4.7586835E−3	1.5985379E−4	−2.1429977E−4	−4.4257744E−3	−2.7057990E−3	4.4621407E−4
c_3	−3.3569963E−6	−4.9286471E−7	−1.1444930E−6	0.0	0.0	−9.1080591E−7
c_4	0.0	0.0	0.0	1.9572733	1.4119239E−1	0.0
c_5	−1.3179396	0.0	0.0	0.0	0.0	0.0
c_6	−3.8389101E−6	−2.7855285E−7	−1.1558081E−7	2.4223436E−6	8.1132965E−7	1.0647399E−7
c_7	0.0	1.1877015E−9	1.1952370E−9	0.0	0.0	2.4273357E−10
c_8	2.2815104E−3	0.0	0.0	−9.3796135E−4	−1.1453082E−4	0.0
c_9	0.0	0.0	0.0	−1.5026030	2.3895671	3.5874255E−1
c_{10}	0.0	0.0	0.0	3.0272240E−3	5.0527457E−4	6.3319710E−5
c_{11}	0.0	0.0	0.0	−31.377342	−17.763460	−249.89661
c_{12}		−96.539512	−221.34306	−12.847063	985.92232	0.0
c_{13}		4.4774938E−1	0.0	0.0	0.0	0.0
c_{14}		101.81078	71.820393	0.0	0.0	888.76800
c_{15}		5.3783879E−6	6.6089246E−6	−1.5056648E−5	−5.4965256E−7	−6.6348003E−7

The new parameters in Table 3.5 can be used at the temperature range 274 – 303 K. Combining equations (3.2), (3.18) and (3.19), Equation (3.26) is obtained.

$$n_{CO2,total} = n_{CO2,hydrate} + n_{CO2,water} \qquad (3.26)$$

$$n_{CO_2,total} = \left(\frac{P_{CO2}}{RT}\right) \cdot (V_{total} - V_{liquid} - V_{hydrate}) + \\ + n_{hydrate} + m_{CO2} (n_{H_2O,total} - n_{H_2O,hydrate}) \qquad (3.27)$$

Table 3.5 Constants to Calculate T-P Coefficient in Equation (3.25)

T-P coefficient	$\frac{\mu_{CO_2}^{l(0)}}{RT}$
c_1	134.72067
c_2	-3.6727291E-1
c_3	-14132.405
c_4	4.7809063E-4
c_5	-5622.8080
c_6	7.9181559E-2
c_7	-1.2283602E-2
c_8	-2.9597665
c_9	6.5155997E-1
c_{10}	7.4901468E-4

The conversion model for CO_2 hydrate at HLV equilibrium is expressed as:

$$\begin{aligned} n_{hydrate} = n_{CO_2,total} - \left(\frac{P_{CO2}}{RT}\right)(V_{total} - V_{liquid} - V_{hydrate}) - \\ - m_{CO2}(n_{H_2O,total} - n_{H_2O,hydrate}) \end{aligned} \qquad (3.28)$$

Rui Sun and Zhenhao Duan (2005) indicate that the mole volume of structure I hydrate (CO_2 hydrate belongs to structure I hydrate) can be expressed as:

$$\begin{aligned} v_w^\beta(T,P) = (11.818 - 9.0871\times10^{-5}T + 3.9468\times10^{-6}T^2 - 4.7254\times10^{-9}T^3 - \\ 8.4133\times10^{-4}\cdot P + 1.5207\times10^{-6}P^2 - 2.2\times10^{-9}P^3)^3\,\frac{10^{-30}\cdot N_A}{N_w^\beta} \end{aligned} \qquad (3.29)$$

where v_w^β is mole volume of CO_2 hydrate .

In Equation (3.29), N_A is the Avogardro's number, N_w^β is the number of water molecules per hydrate cell. For structure I hydrate, N_w^β equals 46. T is temperature in K. P is pressure in MPa.

Combining equations (3.2), (3.18) and (3.29), Equation (3.30) is obtained:

$$V_{hydrate} = n_{hydrate} \times v_w^\beta \qquad (3.30)$$

Combining equations (3.28) and (3.30), we can get:

$$n_{hydrate} = \frac{n_{CO_2,total} - (\frac{P_{CO2}}{RT}) \cdot V_{total} + (\frac{P_{CO2}}{RT}) \cdot V_{liquid} - m_{CO_2}(n_{H_2O,total} - n_{H_2O,hydrate})}{1 - \frac{P_{CO2} \cdot v_w^{\beta}}{RT}} \quad (3.31)$$

From Equation (18) we can get:

$$n_{H_2O,hydrate} = n \times n_{hydrate} \quad (3.32)$$

From Equation (3.1), *n* equals 6.2. Combining equations (3.31) and (3.32), we obtained:

$$n_{hydrate} = \frac{n_{CO_2,total} - (\frac{P_{CO2}}{RT}) \cdot V_{total} + (\frac{P_{CO2}}{RT}) \cdot V_{liquid} - m_{CO_2} n_{H_2O,total}}{1 - \frac{P_{CO2} \cdot v_w^{\beta}}{RT} - 6.2 m_{CO_2}} \quad (3.33)$$

In Equation (3.33), V_{liquid} is determined by Equation (3.3) that combined with Equation (3.18) gives:

$$V_{liquid} = \frac{(n_{H_2O,total} - 6.2 \cdot n_{hydrate})}{\rho_{liquid}} \cdot M_{H_2O} \quad (3.34)$$

Combining (3.33) and (3.34)

$$n_{hydrate} = \frac{n_{CO_2,total} - (\frac{P_{CO2}}{RT}) \cdot V_{total} + (\frac{P_{CO2}}{RT}) \frac{n_{CO_2,total} \cdot M_{H_2O}}{\rho_{liquid}} - m_{CO_2} * n_{H_2O,total}}{1 - \frac{P_{CO2} \cdot v_w^{\beta}}{RT} - 6.2 m_{CO_2} + 6.2(\frac{P_{CO2}}{RT}) \frac{M_{H_2O}}{\rho_{liquid}}}$$

(3.35)

Knowing the total mole volume of the reactor, the total mole volume of water and total mole volume of gas, Equation (3.35) can be used to calculate the total mole of hydrate. This equation is suitable for both open system and for HLV equilibrium state.

4. The Experimental Approach

4.1 CO_2 Hydrate Slurry Production System with Compressor

The experimental rig comprises a hydrate production unit, a hydrate consumer unit installed in a climate room, see Figure 4.1. Figure 4.2 shows a schematic representation of the overall system that is made up of three different circuits, namely the hydrate production loop (in black), the CO_2 gas circuit (in red) and Neutragel/Water coolant circuits (in blue). Detailed information of the different components is provided in tables 4.1 to 4.3.

The main objective of this research is using different experimental devices with different experimental configurations in order to study the production, distribution and consumption of CO_2 hydrate slurry.

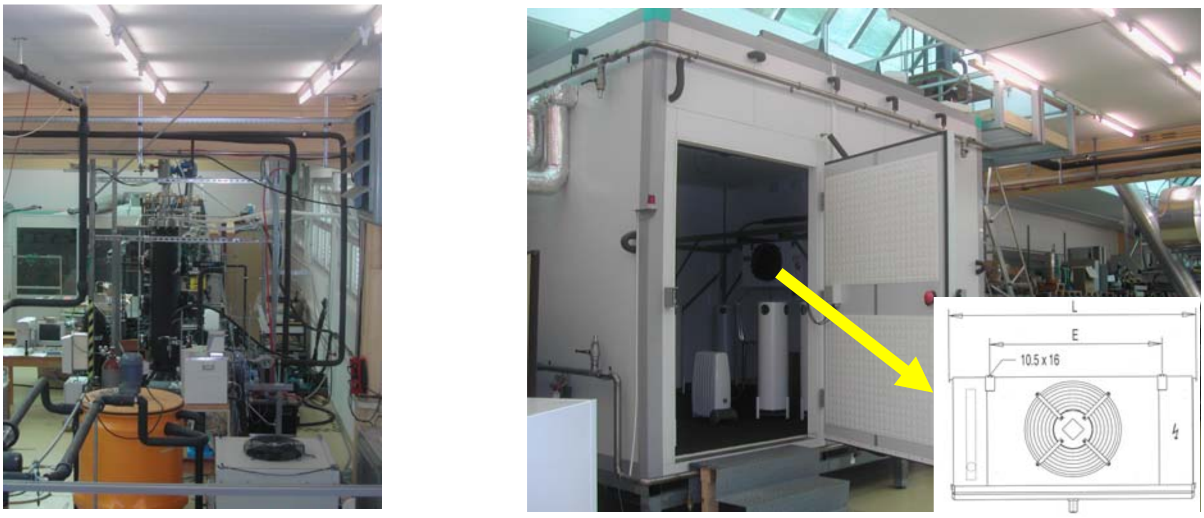

a) Hydrate Production Unit b) Climate Room with Hydrate Consumer Unit

Figure 4.1: The CO_2 Hydrate Slurry Experimental Rig

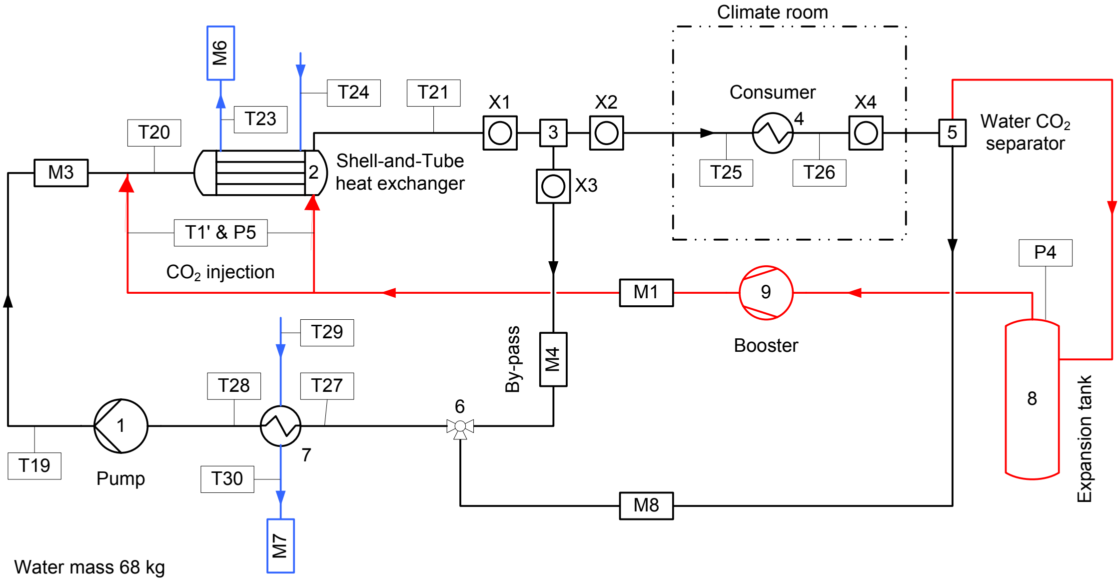

Water mass 68 kg
CO_2 mass 14 kg
Pressure at ambient temperature 32 bar
Operating pressure 27 bar

Figure 4.2: Schematic Representation of the CO_2 Hydrate Slurry System with Compressor

CO_2 hydrate slurry loop (in black)

This loop is totally made up of stainless steel tubes to withstand a pressure of 40 bar. It comprises one pump (1), one shell-and-tube heat exchanger (2), four visualization windows (X_1 to X_4), one hydrate consumer (4) and one mixing valve (6). It also incorporates three mass flow meters that monitor the mass flow rate, the density as well as the viscosity. Temperatures are measured with seven PT100 sensors. For comparison purposes, two injection points where set up, before and after the shell-and-tube heat exchanger (2). Window X_1 allows visual inspection of the hydrate slurry quality and mass fraction. Diverter 3 allows splitting of the incoming flow into the three-way valve (6) to guarantee a constant flow rate supply to the pump. The remaining hydrate slurry heads to the consumer in the climate room, situated about 15 m way from the divider. At the exit of the consumer, window X_4 is installed allowing observation of the hydrate slurry phase change. From here the hydrate slurry and/or the CO_2 solution leaves the climate room and enters a water-gas separator (5) where the CO_2 gas and CO_2 solution are separated.

CO_2 gas circuit (in red)

The CO_2 gas extracted at the top of the water-gas separator (5) is then directed into a tank (8) where it is compressed in order to be once again injected into the gas circuit.

Neutragel/Water cooling loops (in blue) for the shell side of heat exchanger.

Since creation of hydrates is an exothermic process, two chillers are used in the loop to cool down the temperature of the CO_2 solution. The chillers (not displayed in the above figures) work with a Neutragel/Water 30% mixture and each coolant loop is monitored by one mass flow meter and two PT100 sensors.

Table 4.1 Technical Information of Different Components

N°	Description	Manufacturer	Model
1	High pressure pump	Sterling	AEHA 1201ABAF3 4B 4
2	Heat Exchanger	Axima	High pressure, 1 pass, shell and tube
3	Hydrate separator		
4	Heater	Güntner	S-GGHF 040.1C/17-AW/20P
5	Water CO2 separator	TiS	
6	By-pass regulator	Kohler	
7	Heat Exchanger	TiS	High pressure, 1 pass, shell and tube
8	Expansion tank	TiS	
9	Booster	Bauer	Compressor
M1	Mass flow meter	Endress+Hauser	Promass 63AS02
M3	Mass flow meter	Endress+Hauser	Promass 83I25
M4	Mass flow meter	Endress+Hauser	Promass 83I25
M6	Mass flow meter	Endress+Hauser	Promass 63FS25
M7	Mass flow meter	Endress+Hauser	Promass 63FS40
M8	Mass flow meter	Endress+Hauser	Promass 83F15
P4	Pressure transducer	Wika	Type S-10 0…40 bar G1/2B
P5	Pressure transducer	Wika	Type S-10 0…100 bar G1/2B
T19…30	Thermocouple	Roth	PT100
T1'	Thermocouple	Roth	K-type

Table 4.2 Nomenclature for the CO_2 Hydrate Slurry Monitoring Loop

Component	**Description**
T_{19}	Temperature at the outlet of the pump 1
T_{20}	Temperature at the inlet of the heat exchanger 2
T_{21}	Temperature at the outlet of the heat exchanger 2
T_{25}	Temperature at the inlet of heater 4
T_{26}	Temperature at the outlet of heater 4
T_{27}	Temperature at the inlet of heat exchanger 7
T_{28}	Temperature at the outlet of heat exchanger 7
M_3	Mass flow rate density and viscosity at the inlet of heat exchanger 2
M_4	Mass flow rate density and viscosity in the by-pass
M_8	Mass flow rate at the outlet of consumer 4
P_4	Loop pressure
X_1, X_2, X_3, X_4	Visualisation windows

Table 4.3 Nomenclature for the Neutragel/Water Monitoring Loops

Description	**Heat Exchanger 2**	**Heat Exchanger 7**
Silicon oil inlet temperature	T_{24}	T_{23}
Silicon oil outlet temperature	T_{29}	T_{30}
Mass flow rate at shell side of heat exchangers	M_6	M_7

4.2 CO_2 Hydrate Slurry Production System without Compressor

The experimental rig employed to generate the CO_2 hydrate slurry consists of three main systems, see Figure 4.3. The objective of this experimental rig is to create CO_2 hydrate slurry without compressor by only cooling the heat exchangers to create hydrates in order to approach industrial systems.

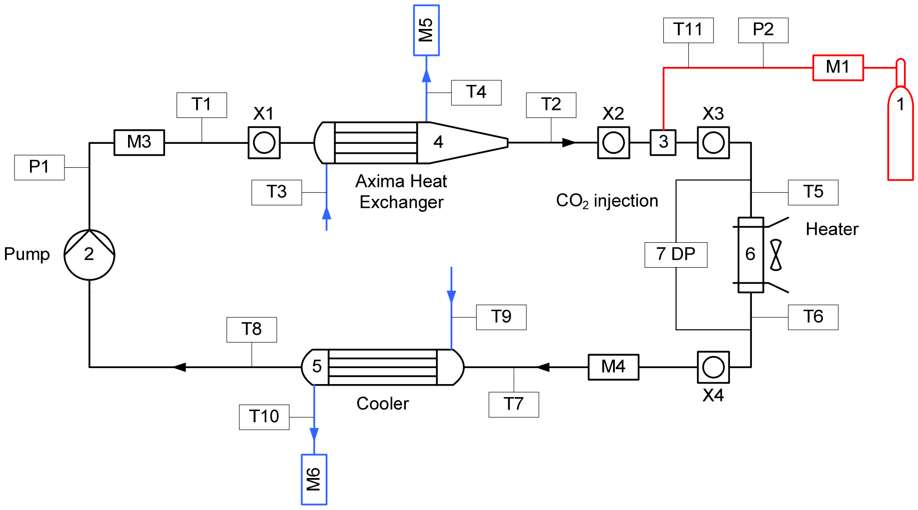

Figure 4.3 Schematic Representation of the CO_2 Hydrate Slurry System without Compressor

CO_2 hydrate slurry loop (in black)

It is equipped with a high-pressure pump (2), two shell-and-tube heat exchangers (4 and 5), one heater (6) and CO_2 gas injection unit (3). Among the two heat exchangers, (4) will be used for hydrate production and (5) will be used as a cooler to cool down the temperature. This loop is monitored by: six PT100 sensors for temperature at different locations; two mass flow meters for mass flow rate, density and temperature of the fluid; one pressure transducer for the loop pressure; one differential pressure flow meter (7) to measure pressure drop of heater (6) and four visualisation windows (X_1 to X_4), see tables 4.4 to 4.5.

CO_2 gas circuit (in red)

One CO_2 bottle feeds the gas circuit to the one single injection point of the CO_2 hydrate slurry loop. Gas temperature is monitored by one K-type thermocouple (T_{11}), pressure is recorded by transducer (P_2) and mass flow rate is recorded by mass flow meter (M_1).

Table 4.4 Technical Information of Different Components

N°	Description	Manufacturer	Model
1	CO2 bottle	Carbagas	
2	High pressure pump	Sterling	AEHA 1201ABAF3 4B 4
3	Gas injection	TiS	
4	Heat Exchanger	Axima	High pressure, 1 pass, shell and tube
5	Heat Exchanger	TiS	High pressure, 1 pass, shell and tube
6	Heater	Güntner	S-GGHF 040.1C/17-AW/20P
M1	Mass flow meter	Endress+Hauser	Promass 63AS02
M3	Mass flow meter	Endress+Hauser	Promass 83F15
M4	Mass flow meter	Endress+Hauser	Promass 83I25
M5	Mass flow meter	Endress+Hauser	Promass 63FS25
M6	Mass flow meter	Endress+Hauser	Promass 63FS40
P1	Pressure transducer	Wika	Type S-10 0…40 bar G1/2B
P2	Pressure transducer	Wika	Type S-10 0…100 bar G1/2B
T1…10	Thermocouple	Roth	PT100
T11	Thermocouple	Roth	K-type

Table 4.5 Nomenclature for the CO_2 Hydrate Slurry Monitoring Loop

Component	**Description**
T_1	Temperature at the inlet of heat exchanger 4
T_2	Temperature at the outlet of heat exchanger 4
T_5	Temperature at the inlet of heater 6
T_6	Temperature at the outlet of heater 6
T_7	Temperature at the inlet of heat exchanger 5
T_8	Temperature at the outlet of heat exchanger 5
M_3	Mass flow rate and temperature at the inlet of heat exchanger 4
M_4	Density and temperature at the inlet of heat exchanger 5
P_1	Loop pressure
X_1, X_2, X_3, X_4	Visualisation windows
DP-7	Differential pressure flow meter

Neutragel/Water cooling loops (in blue) for shell side of two heat exchangers

There are two chillers (not displayed in Figure 4.3) using Neutragel/Water 30% as coolant to cool down (or heat up) the two heat exchangers (4) and (5); each coolant loop is monitored by one mass flow meter and two PT100 sensors, see Table 4.6. Two Sulzer SMV type gas mixers, see Figure 4.4, are placed in the hydrate production loop to aid the mixing of CO_2 gas with water.

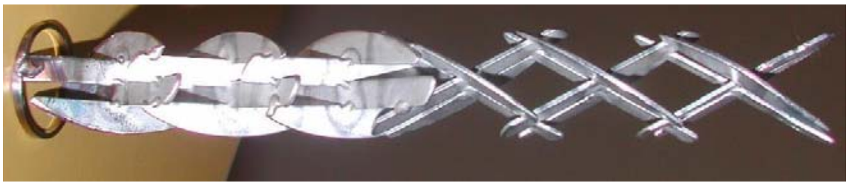

Figure 4.4 Sulzer SMV Gas Mixer

One is located just after the CO_2 gas injection point (3) allowing the large CO_2 gas bubbles generated at the injection nozzle to be dispersed and form very fine and uniform bubbles. As the gas bubble surface area is greatly increased, the hydrate formation speed is also greatly enhanced. The second static mixer is situated after visualization window X_1 and before the inlet of Axima heat exchanger. This static mixer acts as a pre-mixing unit for the CO_2 solution before going through the tubes of the Axima heat exchanger.

Table 4.6 Nomenclature for the Neutragel/Water Monitoring Loops

Description	Heat Exchanger 4	Heat Exchanger 5
Neutragel/Water inlet temperature	T_3	T_9
Neutragel/Water outlet temperature	T_4	T_{10}
Mass flow rate at shell side of heat exchangers	M_5	M_6

4.2.1 CO_2 Hydrate Slurry Production Unit: Axima Heat Exchanger

To simplify the CO_2 hydrate slurry production system and reduce the cost, heat exchangers will be used to produce the hydrate slurry directly and continuously. Our previous experimental results showed that the conventional shell-and-tube heat exchanger is not adequate for hydrate production. The formation rate was low and the head of the heat exchanger was easily blocked by hydrate agglomeration.

To prevent hydrate blockage at the head of the heat exchanger, the original hemispherical head of the heat exchanger was replaced by a conical head. Experimental results have shown that the new head design can greatly reduce the possibility for hydrate blockage.

In addition, to improve hydrate formation in the tubes of Axima heat exchanger, twenty one Kenics static mixers were placed in the tubes of this heat exchanger, each one with a length of 1.5 m and 13.5 mm outer diameter.

Figure 4.5 Kenics Static Mixer

Each static mixer has 62 elements. Figure 4.5 shows a Kenics static mixer mounted in an adaptor pipe. The mixer section consists of right handed helical elements connected to left-handed helical elements that are rotated by 90°.

Figure 4.6 shows the flow divisions produced by the elements in the Kenics mixer and their effect on the radial distribution of two different materials. It can be seen that each mixer divides the stream into two layers and rotates them 180°.

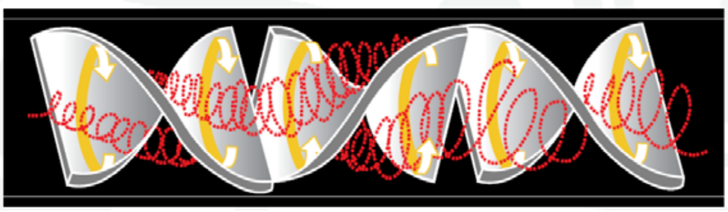

Figure 4.6 Operation Principles of the Kenics Static Mixer

The number of layers generated through this process, which is a measure of the mixing taking place, can be estimated from the equation proposed by Donald E. De Laney *et al.* (2004):

$$S = 2^E \qquad (4.1)$$

where S is the total number of layers and E is the number of elements in the static mixer.

According to Equation (4.1), a Kenics static mixer of 62 elements will subdivide a melt stream by $4.6 * 10^{18}$ times to produce excellent dispersive as well as distributive mixing of the melt. CO_2 gases can be incorporated into turbulent liquids using the Kenics static mixer. Mass transfer rates are dramatically enhanced to maximize absorption or reaction.

4.3 Measurement Techniques

4.3.1 Measurement of Temperature

A new temperature sensor was developed in collaboration with Roth + CO AG. The objective was to obtain a high precision temperature measurement in a point. The sensor diameter is 2 mm and the sensitive layer is 1.6 mm high by 1.2 mm long, see figures 4.7a and 4.7b.

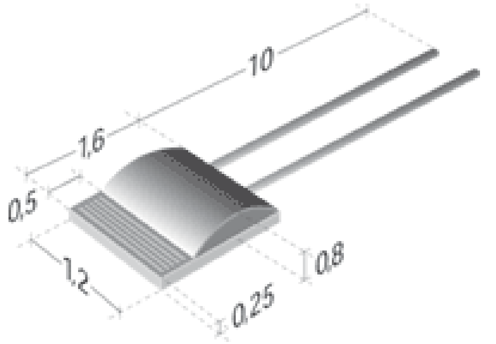

Figure 4.7a Temperature Sensor PT100

Figure 4.7b Geometry of the Mini- Sensor

4.3.2 Measurement of Mass Flow Rate

Mass flow rate of all working fluids in the experimental rig were measured by Endress+Hauser mass flow meters.

4.3.3 Measurement of the Fluid Density

Densities of CO_2 solution as well as CO_2 hydrate slurry are measured by mass flow meters of Endress+Hauser which were calibrated according to the suitable temperature and pressure range for hydrate formation and dissociation.

4.3.4 Measurement of the Heat Capacity and Enthalpy

Heat capacity and enthalpy are determinated by a digital scanning calorimetry (DSC). The specifications identified for the development of the new DSC calorimeter are the following:

- Range of temperatures: -50 °C to 50 °C
- Range of pressures: 0 to 400 bar
- Volume of the sample: at least 50 µl
- Duration of experiment: 1 to 2 days
- Miscellaneous: hardiness, reliability

The base calorimeter was selected to be easily adapted and modified to meet the whole specifications previously described: Micro DSCVII by Setaram. The calorimetric furnace is made of a double aluminium wall, see Figure 4.8. The experimental and reference vessels are inserted into the furnace by two cylindrical cavities. The main advantage relates to the system of cooling, which is provided by Peltier effect. This system avoids the handling of refrigerating fluids such as liquid nitrogen. The minimum temperature that can be reached is about –45 °C and the maximum temperature is 120 °C.

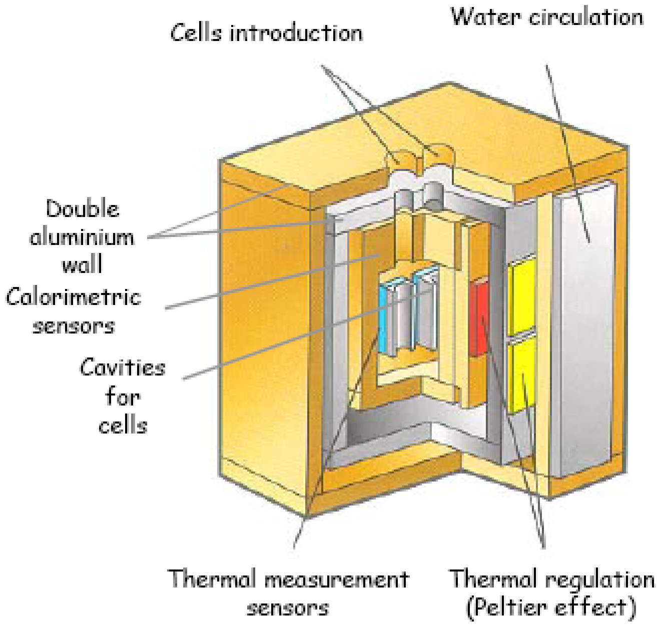

Figure 4.8 Schematic of SETARAM Micro DSCVII Calorimeter

The working principle of Micro DSCVII

In the heat flux DSC (a Tian-Calvet type microcalorimeter), thermal effects are measured by two fluxmeters (one on the measurement side and one on the reference side), each of which measures the thermal power exchanged at each moment between the vessel and the calorimetric unit. The Tian-Calvet fluxmetric transducer envelopes the sample, making it possible to measure almost all the exchanges between the vessel and the unit. The differential power required to heat the sample compared to the reference at the same scan rate is thus recorded. This capability gives this device a clear metrological advantage in terms of the quantity of measurements and their sensitivity, see Figure 4.9.

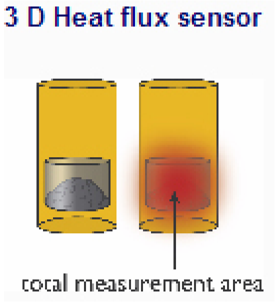

Figure 4.9 Schematic of DSC Working Principle

Definition of high-pressure vessels

Specific vessels able to support high pressures up to 400 bar were specially designed, see Figure 4.10. They are made of alloy Hastelloy C276, the maximum working volume is 0.5 ml. The high-pressure vessels can be re-used after a suitable cleaning.

Figure 4.10 Specific High-Pressure Vessel

Handling of high-pressure vessels

The high sensitivity of the Micro DSCVII calorimeter requires a meticulous cleaning of vessels between each analysis, before and after the filling with the sample. Humidity or finger traces on the walls or in the sealing system can lead to thermal signals of interference during the analysis. Classically, vessels are filled by means of a spatula in the case of solids or a pipette in the case of liquids. The vessel has to be weighted before and after filling, in order to precisely determine the mass of sample to be analysed. The reference vessel can be empty or filled with an inert material in order to compensate for the differences in heat capacity between the two vessels. The inert material can be alumina (for powders) or silicone oil (for liquids).

Heat Capacity

Heat capacity of water was determined by the Continuous method. This method can only be applied to instruments calibrated by Joule effect such as DSC111, DSC121, C80, HT1000, BT215, Micro DSCIII and Micro DSCVII. The method consists in performing two runs with two vessels: the measuring vessel and the reference vessel. The first run is performed with the two empty vessels (blank test), the second run with a mass m_S of sample in the measuring vessel. Each run consists in a ramp between an initial temperature T_i and a final temperature T_f at constant heating rate β, see Figure 4.11. If A_b and A_S are the amplitudes measured with the blank and with the sample respectively, the value of specific heat capacity C_P is:

$$\mathrm{Cp} = \frac{A_s - A_b}{m_s \times \beta} \tag{4.2}$$

with C_p in J/g.K, A_s and A_b in W, m_s in g, β in K/s

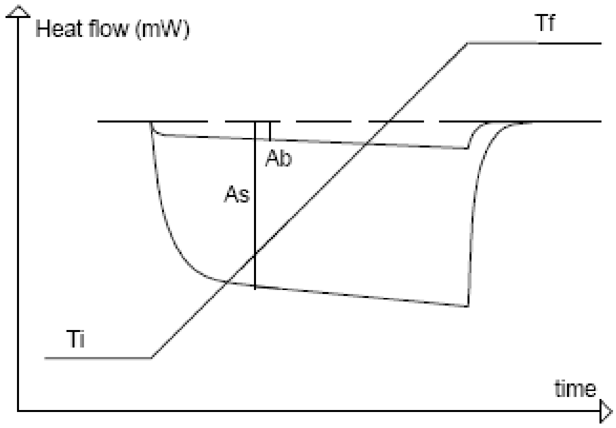

Figure 4.11 Continuous Method to Calculate Cp

4.3.5 Measurement of Dynamic Viscosity of CO_2 Solution and CO_2 Hydrate Slurry

No studies have been reported in the literature regarding viscosity of CO_2 hydrate slurry. The flow properties of CO_2 hydrate slurry are important in understanding hydrate formation-dissociation conditions. They also represent very important reference data in issues such as hydrate transportation, blockage, etc.

Previous experiments indicate that the Endress+Hauser mass flow meter is not adequate for accurate measurements of viscosity of the CO_2 solution and CO_2 hydrate slurry due to the influence of a large amount of accompanying gas bubbles.

Viscosity is a shear measurement and can only be truly assessed under shear conditions, so it was decided to use shear waves. There are many other types of vibrational waves but these are avoided as they can behave unpredictably in process environments. The XL7-100 viscometer produced by Hydramotion Ltd. in UK is in a class of instruments called vibrational or resonant viscometers. Vibrational viscometers work by creating waves, but it turns out that the type of wave is very important. The solid stainless steel sensor element of XL7-100 is submerged in the fluid and made to move back and forth microscopically at a high frequency. This is called “resonance”. As the surface of the sensor shears through the liquid, energy is lost to the fluid because of its viscosity. The dissipated energy is accurately measured by microprocessor-controlled electronics and then equated back to viscosity. Higher viscosity causes a greater loss of energy and hence a higher reading. Due to its overall characteristics the XL7-100 on-line viscometer was selected and it will be used to measure viscosity in our experiments. These set of measurements are scheduled to take place beginning of February 2008.

Specification of Viscometer XL7-100:

Viscosity accuracy: ± 1% of reading

Viscosity repeatability: ± 0.3% of reading

Complete viscosity range: 1-10000 mPa.s

Pressure range: up to 300 bar

Temperature range: -40°C to 150 °C

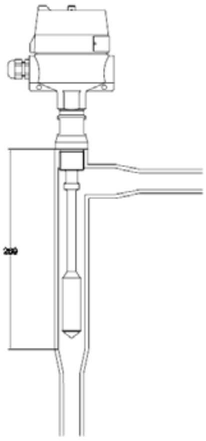

Figure 4.12 Installation of XL7-100 Process Viscometer in the Experimental Loop

4.3.6 Measurement of Corrosion Rate of CO$_2$ Solution and CO$_2$ Hydrate Slurry on Different Materials

The corrosion effects of saturated CO$_2$ solution as well as CO$_2$ hydrate slurry on low carbon steel, stainless steel and copper which are widely used in air-conditioning, cold storage, oil and gas industry were tested in order to evaluate the side effects of using CO$_2$ solution as well as CO$_2$ hydrate slurry as cold carrier. Real-time coupled multielectrode array sensor (CMAS) probes were used to measure the maximum localised corrosion rate of type 1018 low carbon steel, copper 110 and 304L stainless steel in CO$_2$ hydrate slurry and saturated CO$_2$ solution under conditions of temperature range (1 to18 °C), pressure range (25 to 30 bar).

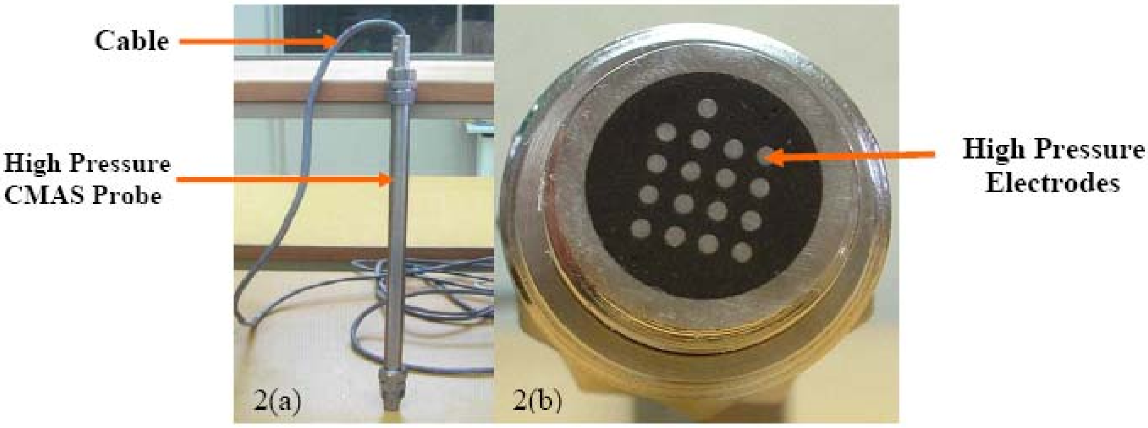

Figure 4.13 High Pressure Coupled Multielectrode Array Sensor (CMAS) Probes (a) and Section of Embedded Electrodes (b)

5. Experimental Results

5.1 Experimental Results of CO_2 Hydrate Slurry Production System with Compressor

5.1.1 Temperature and Pressure Profiles of CO_2 Hydrate Slurry Formation and Dissociation

Figure 5.1 shows the overall temperature and pressure evolution inside the hydrate slurry production loop. During the first 2 hours, the pressure in the tank is seen to decrease despite continuous injection of CO_2 into the system. The reasons are twofold: 1) the transition of CO_2 solution from saturated to super-saturated consumes a large quantity of CO_2 gas (and super saturated CO_2 solution is a necessary condition to form CO_2 hydrate); 2) formation of hydrates also consumes a large amount of CO_2 gas.

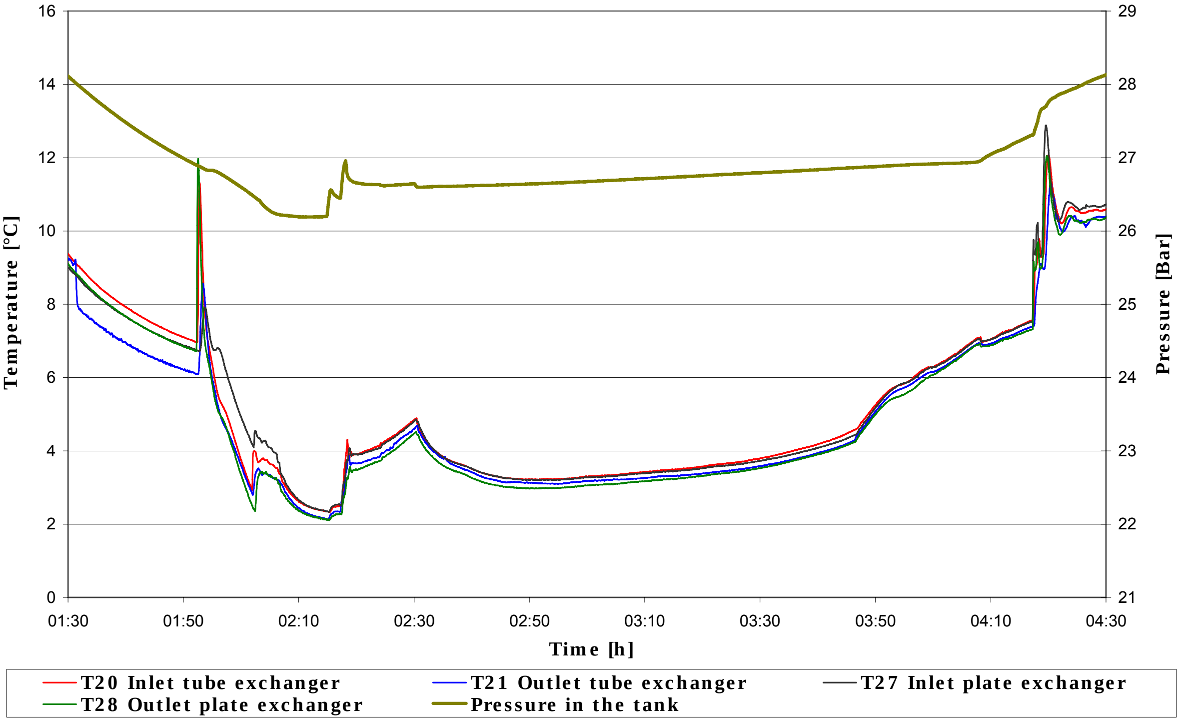

Figure 5.1 Temperature and Pressure Profiles of CO_2 Hydrate Slurry Formation and Dissociation

At 2:15 hours gas injection is stopped and pressure in the tank is seen to gradually increase due to the increase of temperature of the fluid (i.e. the CO_2 gas solubility decreases) when hydrate formation is taking place. About 4:00 hours, a large amount of CO_2 hydrates began to dissociate and a sharp increase of pressure in the tank is observed. Hydrates dissociation releases a huge amount of gas with a consequent increase in system pressure.

Two chillers continuously cooled down the CO_2 hydrate slurry loop. In the first two hours the temperature of the heat exchangers are seen to decrease but as soon as the hydrates start to form, the fluid temperature sharply rises to around 5 °C as a consequence of the exothermic process of hydrate formation and slow response of the heat exchangers to remove this sudden heat of hydrate formation. Only after is the fluid temperature observed to decrease slightly due to the chillers.

The consumer was started to run at maximum power close to 4:00 hours and the CO_2 hydrates started to dissociate as they entered the climate room. As a consequence, the temperature of the fluid passing through two heat exchangers began to increase rapidly (the dissociation is an endothermic process so that the fluid absorbs a considerable amount of heat from the consumer). At 4:15 hours the temperature of the fluid was about 7.5 °C and the hydrates had completely dissociated leaving only the CO_2 solution. As there were no more hydrates in the solution to undergo a phase change, the CO_2 solution temperature was rapidly increase as it absorbed the heat from the consumer, which was still on.

0.1.2 Density of CO_2 Solution and CO_2 Hydrate Slurry

Prior to have CO_2 hydrate slurry, Figure 5.2 shows the density of saturated CO_2 solution reached 1022 kg/m^3 by continuous gas injection. About 2:15 hours, more CO_2 gas was injected, producing a large quantity of gas bubbles that will not be immediately absorbed by the solution and will consequently affect the data acquisition of the mass flow meter. Under these conditions, the mass flow meter showed unstable values, see the sudden density drop displayed in Figure 5.2. Once super saturation of the solution is obtained, CO_2 hydrates began to form very rapidly in the CO_2 solution and the density of the CO_2 hydrate slurry increases very much in just few minutes. At the end of gas injection, density of CO_2 hydrate slurry reached 1031 kg/m^3.

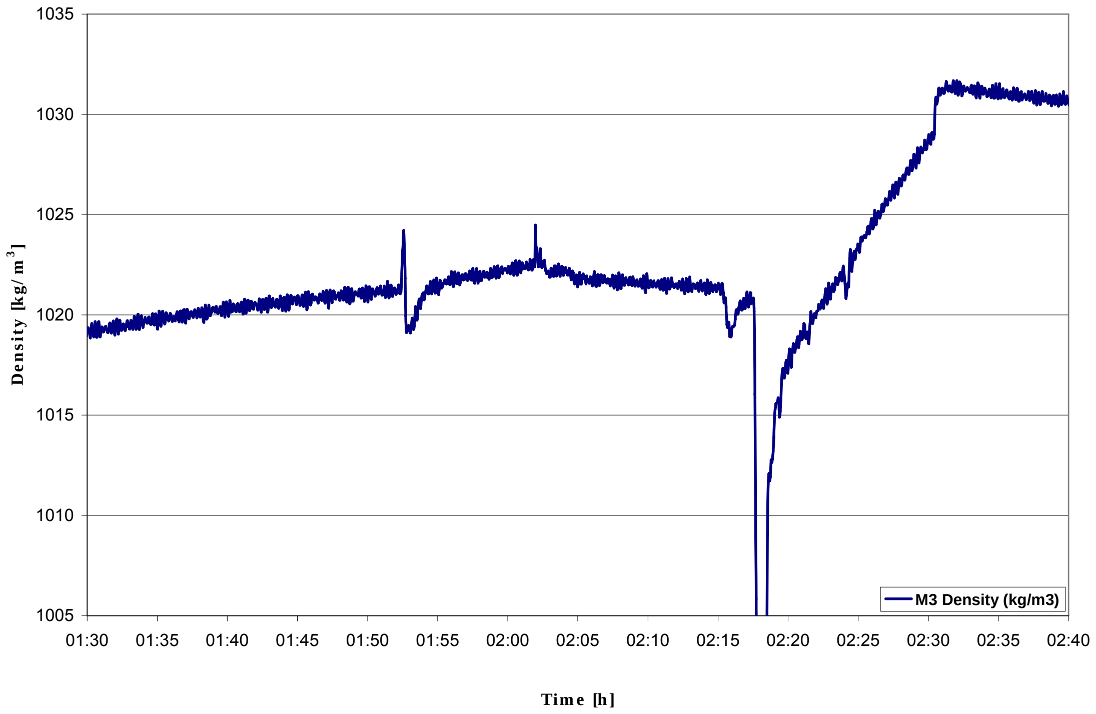

Figure 5.2 The Density Profile of CO_2 Solution and CO_2 Hydrate Slurry

5.1.3 Dynamic Viscosity of CO_2 Solution and CO_2 Hydrate Slurry

Figure 5.3 shows the dynamic viscosity of CO_2 solution and CO_2 hydrate slurry measured by the Endress+Hauser mass flow meter. This was the first approach to the dynamic viscosity measurement.

It can be seen that the dynamic viscosity of CO_2 solution increases when CO_2 solution density increases. The viscosity of CO_2 solution was about 2 mPa.s at 2:15 hours. Further injection of CO_2 gas results in viscosity values not stable due to effect of a large amount of gas bubbles in the system. At steady state, the dynamic viscosity of CO_2 hydrate slurry was about 5 mPa.s.

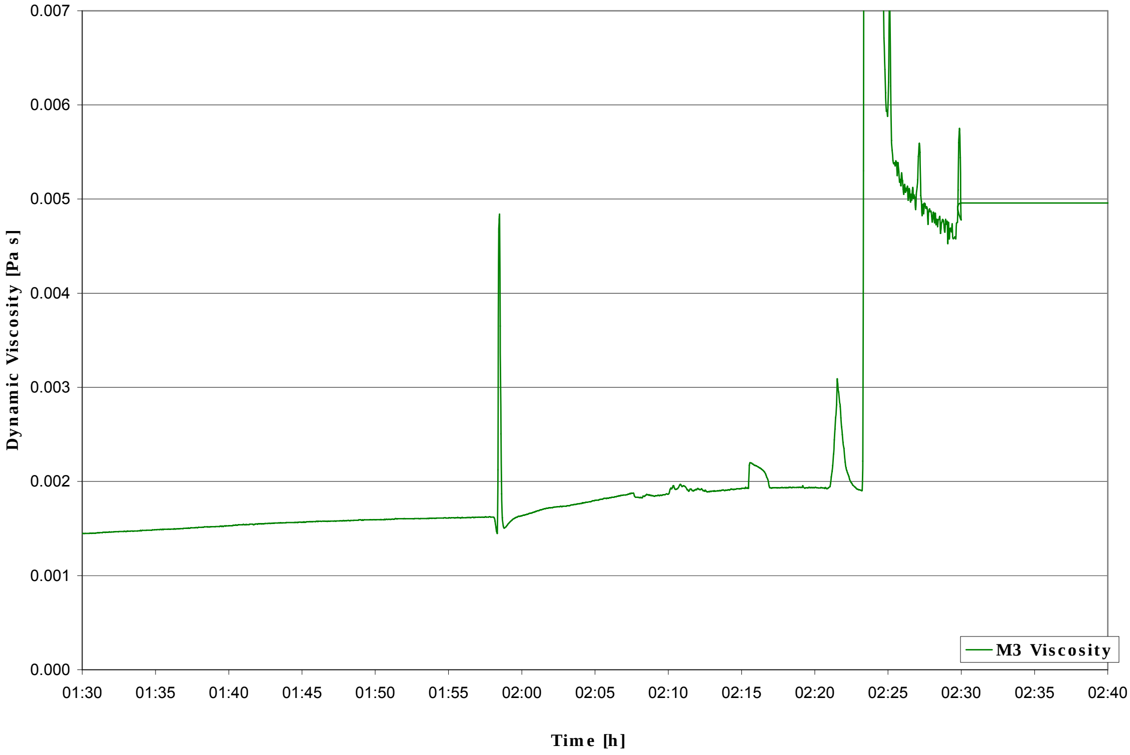

Figure 5.3 Dynamic Viscosity of CO_2 Solution and CO_2 Hydrate Slurry

5.2 Tap Water Test in the New Test Rig without Compressor

5.2.1 Temperature Profiles of the Fluid

The test rig (Figure 4.3) was filled up with tap water for test. Water was first cooled down by two chillers which use Neutragel/Water 30% mixture as coolant. The temperature of two chillers was set at 1 °C for the whole experiment. The function of the two chillers is to cool down the Axima heat exchanger (4) and cooler (5). When the water in the loop was at 2.5 °C, it was left to stabilise for more than 30 minutes. Afterwards, heater (6) was turned on and was run at two different power levels. At each power level, temperature, mass flow rate and power consumption in all loops were monitored while the working conditions for two chillers were kept constant.

Axima heat exchanger is a key component in the CO_2 hydrate slurry loop, see Figure. 4.3. Water flows in the tube side, temperature of water inlet is monitored by T_1; temperature of water outlet is monitored by T_2. Neutragel/Water 30% mixture flows in shell side as coolant. T_3 is the inlet temperature of Neutragel/Water 30% mixture and

T_4 is the outlet temperature of Neutragel/Water 30% mixture. From Figure 5.4 it can be seen that water was first cooled down to 2.5 °C, then heater 6 started to work with a maximum power at beginning. It was observed that temperatures T_1, T_2 and T_4 increased sharply when heater 6 was power on while T_3 remained more or less unchanged. The temperature difference between T_1 and T_2 reached the largest value of 1.6 K. After running for a while, water temperature was seen to go down because the shell side of heat exchanger was continuously cooling by Neutragel/Water 30% mixture. Then the heater was run at another lower power level.

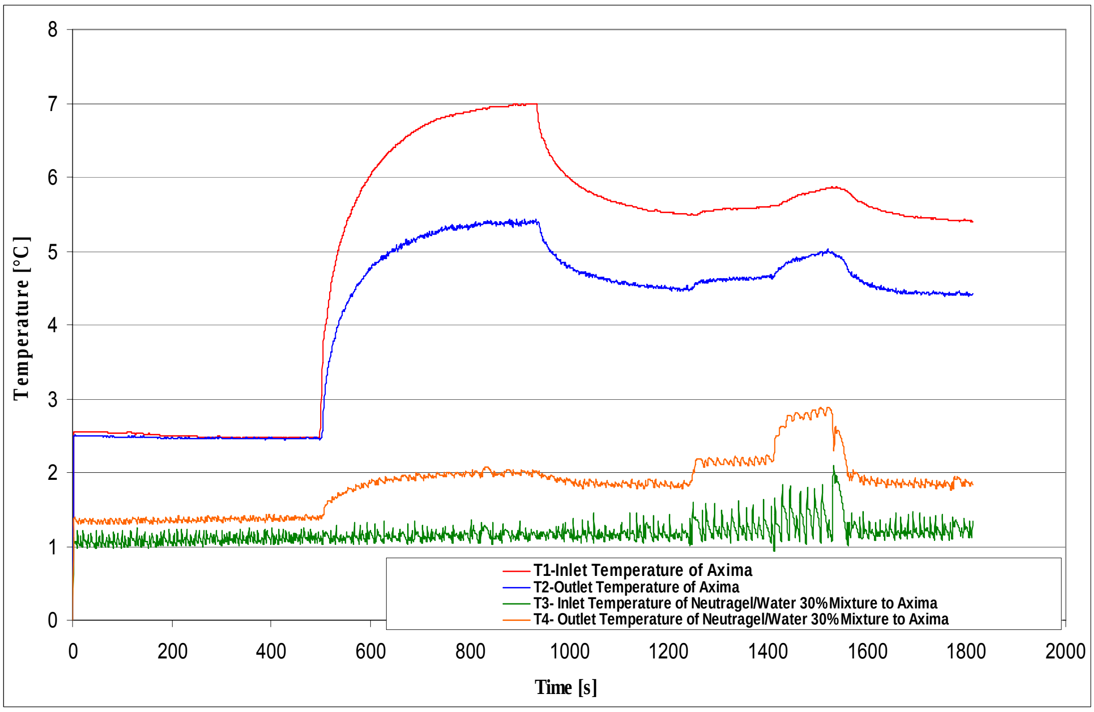

Figure 5.4 Temperature Profile of the Fluids in Axima Heat Exchanger

Figure 5.4 shows that each sudden power change will cause a temperature jump, see the two peaks in Figure 5.4. The temperature difference of T_1 and T_2 is now smaller and has the value of about 1 K. It can also be seen that when the water is first cooled down, the temperature difference between T_3 and T_4 is only 0.2 K. This means that the Neutragel/Water 30% mixture which flows in shell side was not working very well at the beginning of the test. When heater (6) started to work, the temperature difference of water in the tube side began to increase, the temperature difference between T_3 and T_4 was also increased to 0.9 K maximum when the heater (6) was running with maximum power level. From that point on, the temperature difference between T_3 and T_4 decreased slightly to 0.6 K when the heater (6) was running with lower energy level. Nevertheless, the temperature difference between T_3 and T_4 was still following the pattern of the temperature difference between T_1 and T_2.

Cooler (5) is also a type of shell-tube heat exchanger. The purpose of cooler (5) in the CO_2 hydrate slurry loop (see Figure 4.3) is to cool down the temperature of the fluids before entering Axima heat exchanger (4). Water flows in tube side, temperature of water inlet of cooler is monitored by T_7; temperature of water outlet of cooler is monitored by T_8. Neutragel/Water 30% mixture flows in shell side of cooler as coolant. T_9 is inlet temperature of Neutragel/Water 30% mixture to cooler and T_{10} is outlet temperature of Neutragel/Water 30% mixture.

Figure 5.5 shows the temperature difference between T_9 and T_{10} ranges between 0.05 K to 0.2 K during the whole water test. This means Neutragel/Water 30% at the shell side of cooler (5) is not working well. While at the tube side of the cooler, at cooling stage (heater was off) there is about 0.45 K temperature difference between T_7 and T_8. Obviously, water in tube side was affected very much by poor cooling effects of shell side. After the heater started to work at maximum power, the temperature difference between T_7 and T_8 began to increase to maximum 0.8 K. When the heater was running at lower energy level, the temperature difference between T_7 and T_8 began to decrease slightly to 0.7 K.

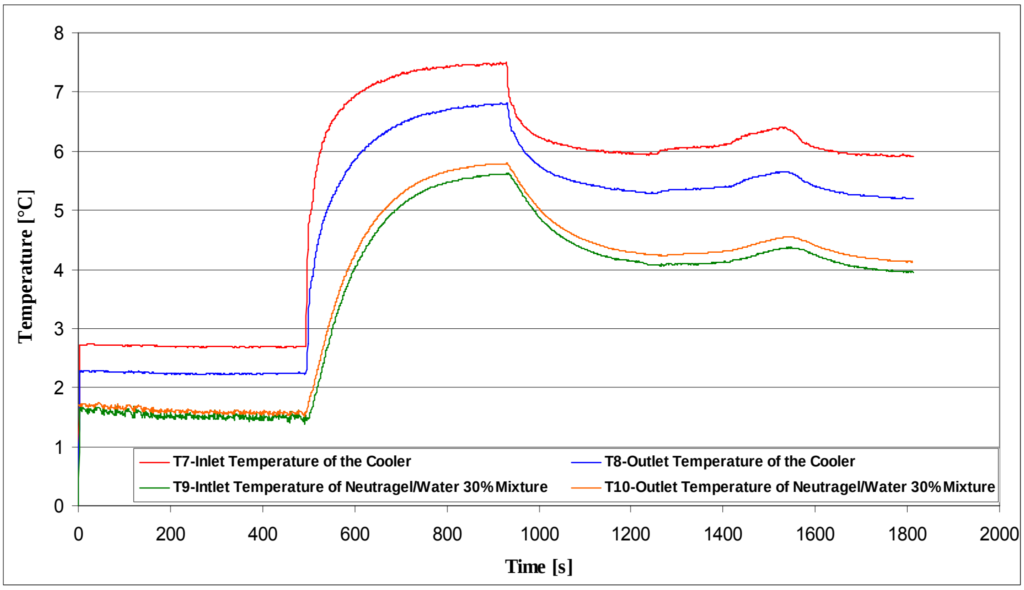

Figure 5.5 Temperature Profile of the Fluids in Cooler (5)

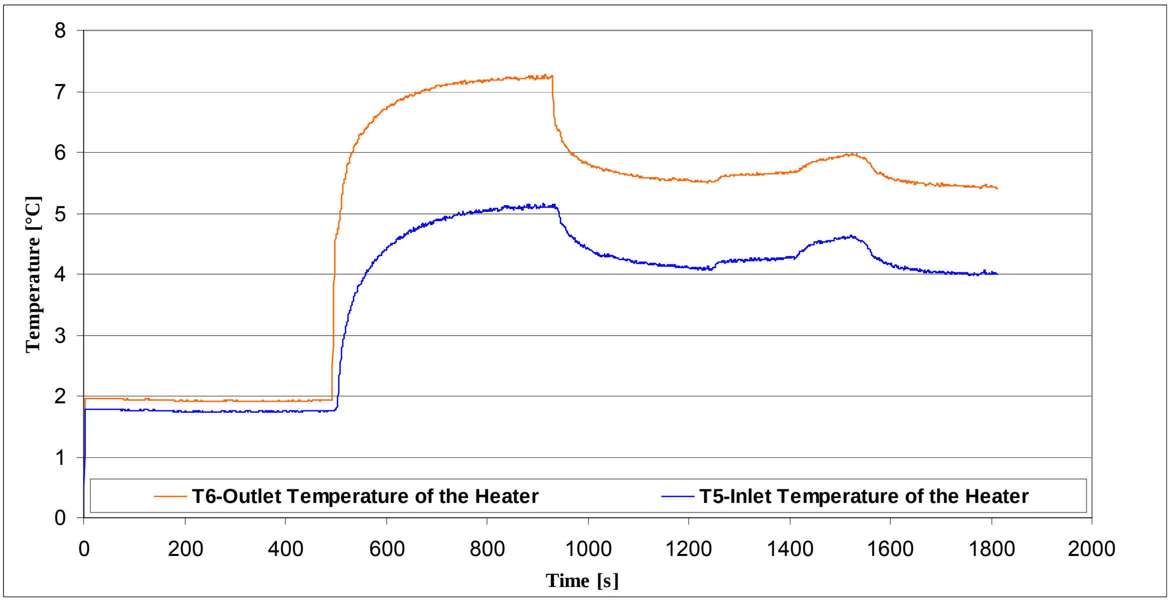

Figure 5.6 Temperature Profile of Heater (6)

Heater (6) in the CO_2 hydrate slurry loop (see Figure 4.3) is used to consume CO_2 hydrates during the hydrates dissociation process. Figure 5.6 shows the temperature profile of heater 6 during the water test. At the beginning of the experiments, the heater was off with only water flow passing through the heater. The temperature difference between T_5 and T_6 was found to be about 0.2 K. After the loop reached the steady state conditions, heater 6 was turned on at two different energy powers. When the heater was turned on at the maximum power level, the temperature difference between T_5 and T_6 increased sharply and was about 2 K. Water temperature was increased by heater. When the heater was running at lower power level, the temperature difference between T_5 and T_6 was about 1.4 K. Figure 5.6 shows the temperature difference between the inlet and outlet of the heater increased when the power of the heater increased.

5.2.2 Mass Flow Rate of Different Fluids in Different Loops

Figure 5.7 shows that during the water test the mass flow rate of water, M_3, was about 0.4 kg/s; mass flow rate of Neutragel/Water, M_5, for Axima heat exchanger (4) was about 1.3 kg/s; mass flow rate of Neutragel/Water, M_6, for cooler (5) was about 1.8 kg/s.

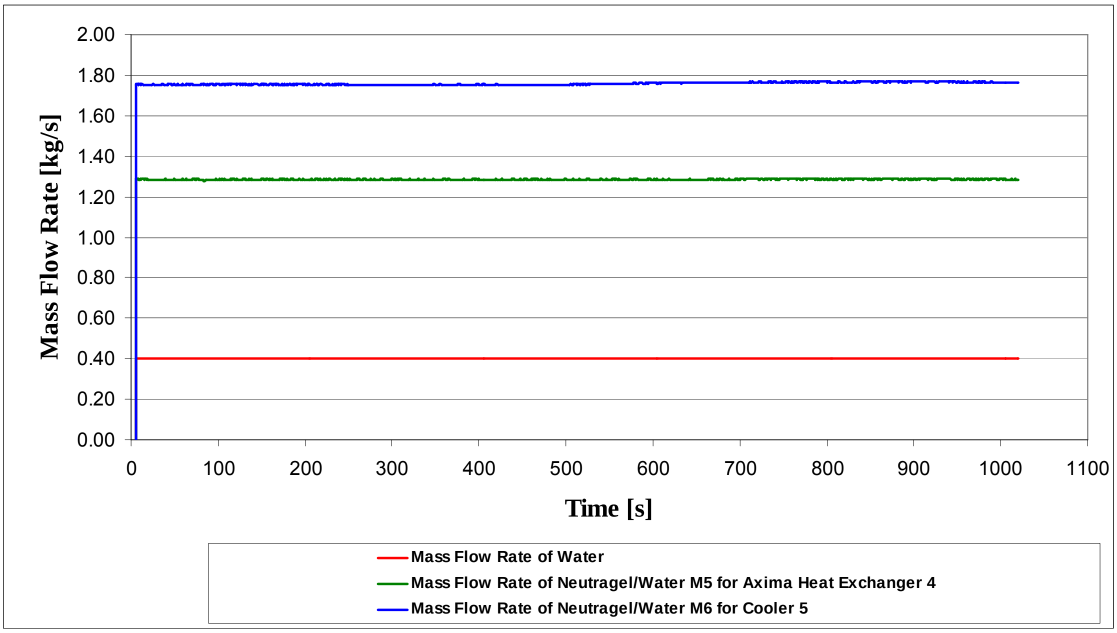

Figure 5.7 Mass Flow Rate of Different Fluids in Different Loops

5.2.3 Energy Balance for Heat Exchangers and Chillers

Due to a number of advantages, most liquid-to-liquid heat exchangers are shell-and-tube type. The high flow rates and heat transfer rates make this type of heat exchanger to be more suitable for most applications than a double pipe heat exchanger. Differences in types of shell-and-tube heat exchangers are based on the flows inside the shell and tubes. Here, Neutragel/Water 30% mixture flows in the shell and water flows in the tubes.

If the water flow or Neutragel/Water 30% mixture flow is unknown, it can be calculated from the global energy balances. As heat storage in the heat exchanger is small compared to the heat transport, the two heat fluxes can be assumed to be equal. In addition, it can also be assumed that: the specific heat capacity (Cp) hot and (Cp) cold are constant; heat loss to the surroundings is negligible and fluid flow is steady state and parallel.

The heat balance can be written in the form of Equation (5.1)

$$\dot{Q} = \dot{m}_h * Cp_h * (T_{hi} - T_{ho}) = \dot{m}_c * Cp_c * (T_{co} - T_{ci}) \qquad (5.1)$$

$\dot{Q}$ = heat transferred from the hot to the cold fluid (kW)

$\dot{m}_h$ = mass flow rate of the hot fluid (kg/s)

Cp_h = specific heat of the hot fluid (kJ/kg.K)

T_{hi} = hot fluid at position inlet (°C)

T_{ho} = hot fluid at position outlet (°C)

$\dot{m}_c$ = mass flow rate of the cold fluid (kg/s)

Cp_c = specific heat of the cold fluid (kJ/kg.K)

T_{co} = cold fluid at position outlet (°C)

T_{ci} = cold fluid at position inlet (°C)

Which is a general form for an ideal heat exchanger (i.e. heat lost by one fluid is equal to heat gained by the second fluid under steady state condition).

Table 5.1 Constants to Calculate Energy Balance between Heat Exchangers and Chillers

Fluids	**Water**	**Neutragel/Water 30% mixture for cooler**
$\dot{m}$ *(kg/s)*	0.4	1.8
Cp (kJ/kg.K)	4.18	3.6

Figure 5.8 shows the calculation results for the cooling power of the cooler (5) (heat exchanger) and its chiller. It can be seen that at steady state, power of Neutragel/Water 30% mixture for cooler (5) is about 1.13 kW, while at the tube side the power is about 1.16 kW, about 3% difference. An acceptable energy balance is obtained. Table 5.1 shows that the mass flow rate of Neutragel/Water 30% mixture for cooler (5) was about 1.8 kg/s. For Axima heat exchanger (4), due to small mass flow rate at tube side (0.4 kg/s), the cooling power provided by Axima heat exchanger (4) was less than the shell side of Neutragel/Water 30% mixture. The energy balance is not reached for Axima heat exchanger (4).

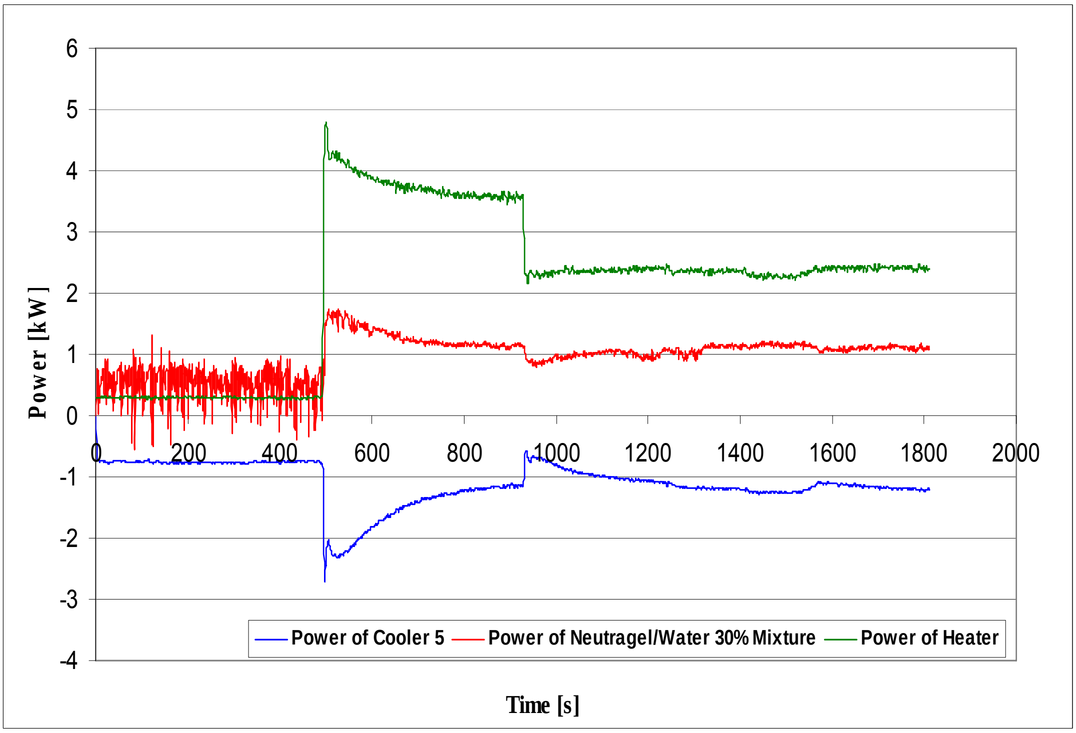

Figure 5.8 Cooling Power of Heat Exchangers and Chillers

5.2.4 Density Measurement

Figure 5.9 shows that during the water density measurement by mass flow meter M_4, the entire loop kept a static pressure of about 4 bar. The mean density value of the measurements from Figure 5.9 was about 1001.2 kg/m^3. Such value was very close to the theoretical calculations reported by Wagner W *et al.* (2000) and Zhang ZG *et al*. (2005) of 1001 kg/ m^3 (at 4 bar, between 2 °C and 8 °C). The deviation of mass flow meter M_4 was very small. The density peak value of 1002 kg/m^3 was due to temperature change in the water when the consumer was running at maximum. Overall the density measurement of water was found to be accurate.

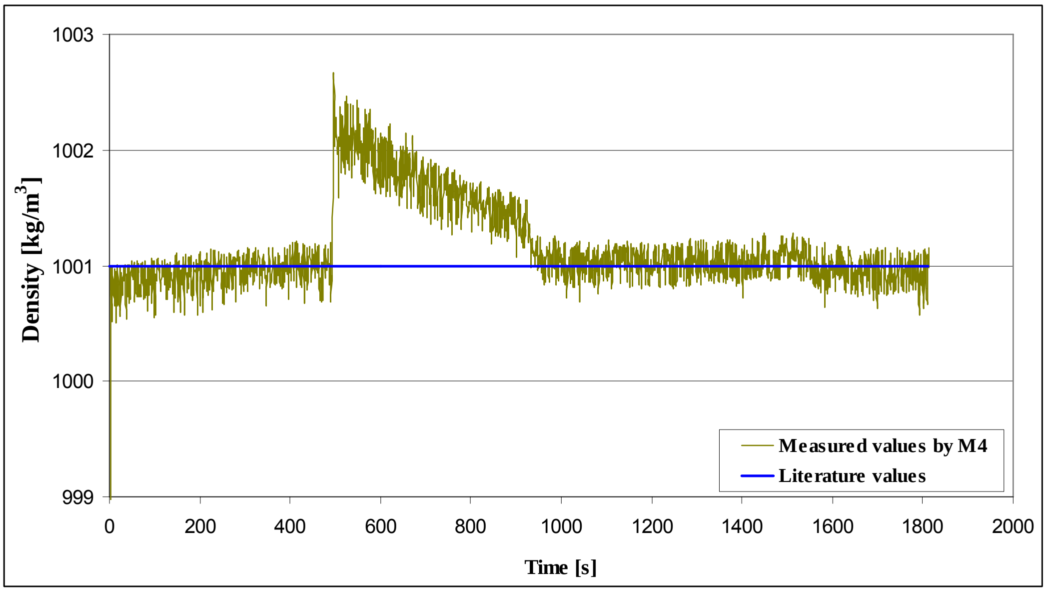

Figure 5.9 Water Density Measurement by Mass Flow Meter M4

5.3 Continuous CO_2 Hydrate Slurry Production in the New Test Rig without Compressor

5.3.1 Temperature and Power Profiles in the Loops

As seen from Figure 5.10, power provided by Neutragel/Water 30% mixture at the shell side of Axima heat exchanger can be obtained from the mass flow rate, Cp and the temperature difference between T3 and T4.

While the power at tube side of Axima heat exchanger could not be obtained at present due to lack of information on the heat capacity of both CO_2 solution and CO_2 hydrates slurry, Figure 5.10 shows that at the cooling stage (first half an hour), the power of Neutragel/Water 30% was rather high. The power even reached 6 kW. Then power sharply dropped down to 1.5 kW when injection of gas began and formed the hydrates. As hydrate formation is an exothermic process, a large amount of heat is released from tube side to shell side at a very short time. Shell side cooling could not follow the speed of heat release, so that the temperature difference between T_3 and T_4 decreased, while the temperature difference between T_3 and T_4 was only about 0.4 K during the whole process. This results in a reduction of the total cooling power. During the whole process of hydrate production, the power was kept more or less constant between 1 to 1.5 kW. The temperature difference between T_1 and T_2 was about 0.2 K during the whole process. The cooling power at tube side of Axima heat exchanger was not enough for fast hydrate creation. Improvement of the heat transfer coefficient at the tube side is of utmost importance.

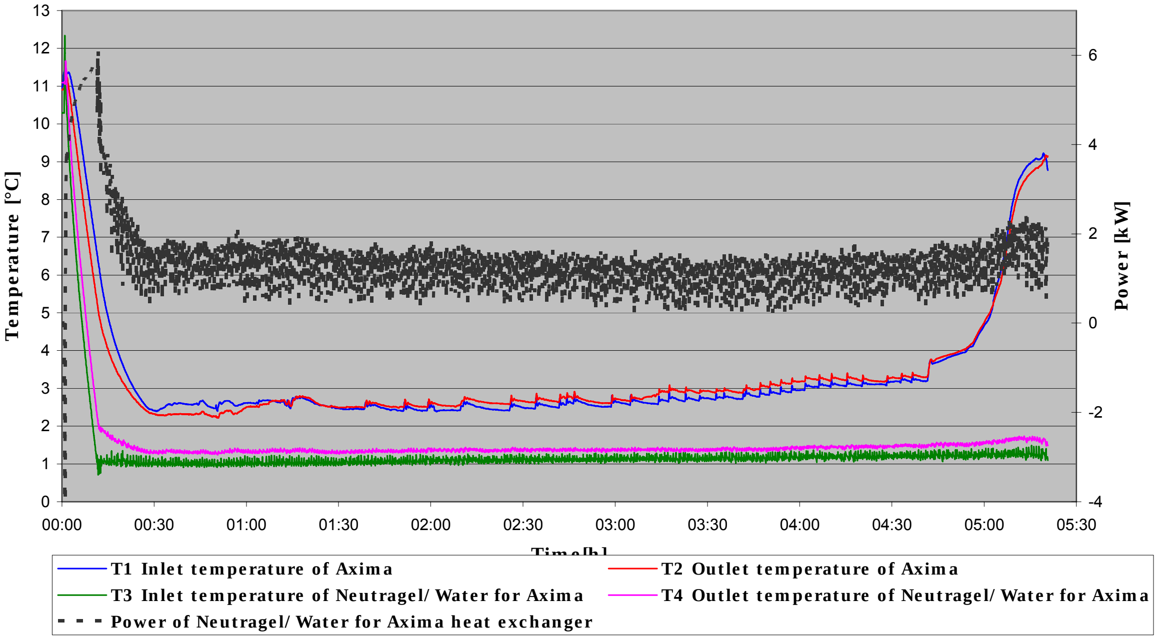

Figure 5.10 Temperature and Power Profiles for Axima Heat Exchanger

As seen from Figure 5.11, power provided by Neutragel/Water 30% mixture at the shell side of cooler can also be obtained from the mass flow rate, Cp and the temperature difference between T_9 and T_{10}. While the power at tube side of Axima heat exchanger could not be obtained at present due to lack of information on the heat capacity of both CO_2 solution and CO_2 hydrates slurry, Figure 5.11 shows that during the overall experiment, the power of Neutragel/Water 30% was very small, less that 1 kW. That means that the chiller which provided such cooling power had some technical problem. The temperature difference between T_9 and T_{10} was only about 0.1 K. There was almost no temperature difference between T_7 and T_8. Cooler (5) did not work well during the production process.

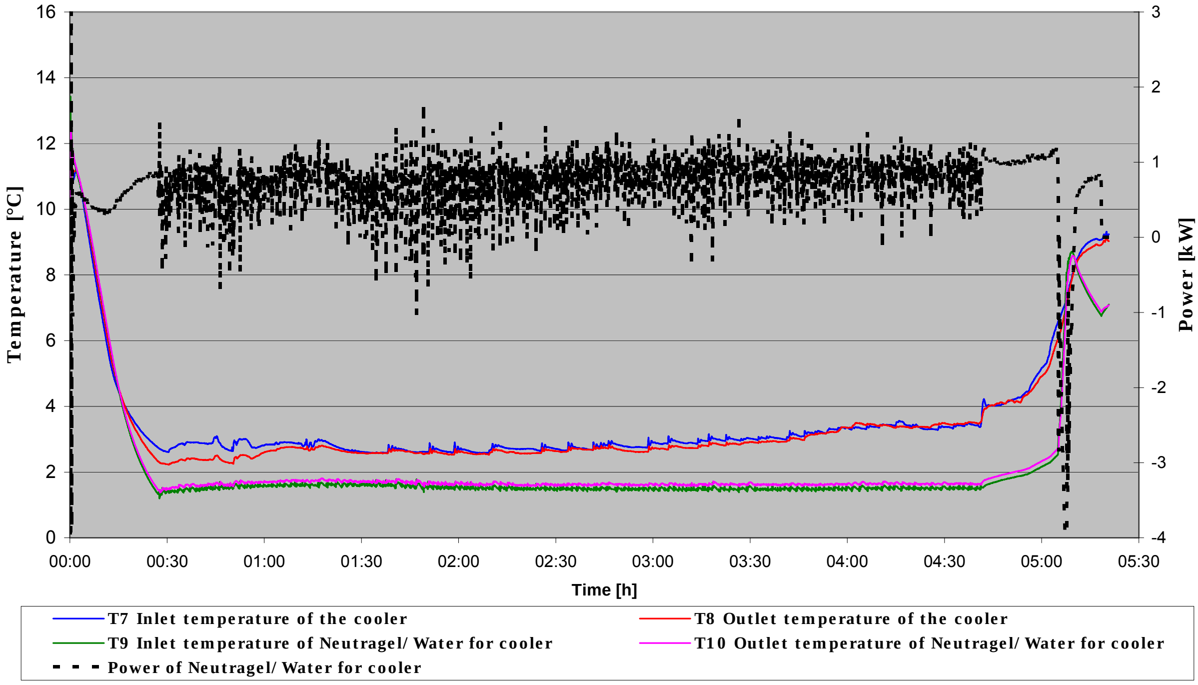

Figure 5.11 Temperature and Power Profiles for Cooler

From Figure 5.12 it can be seen that before 4:30 hours, heater (6) was turned off. The cooling down of the water in the first half hour shows almost no temperature difference between T5 and T6. Then during the period of CO_2 solution and CO_2 hydrate formation, the temperature difference between T5 and T6 was about 0.3 K. After 4:30 hours, the heater was turned on and the mass flow rate of CO_2 hydrate slurry suddenly decreased, the experiment was stopped.

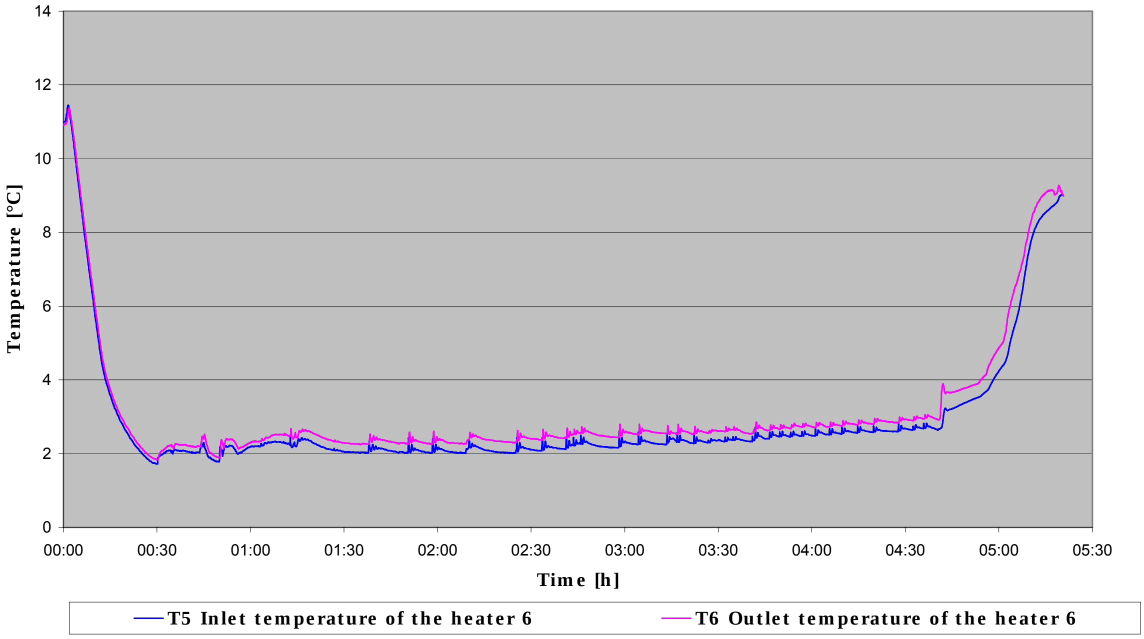

Figure 5.12 Temperature Profile for Heater 6

This is probably due to an increase in the temperature difference between T5 and T6 that caused pressure difference between inlet and outlet of the heater to increase. Pressure drop in the heater (free expansion) will cause hydrate blockage. These assumptions will be tested in the near future.

5.3.2 Mass Flow Rate of Different Fluids

Figure 5.13 shows that during the experiment, the mass flow rate of Neutragel/Water M5 for Axima heat exchanger (4) is about 1.3 kg/s; mass flow rate of Neutragel/Water M6 for cooler (5) is about 1.8 kg/s. Mass flow rates, M_5 and M_6, were kept constant in order to provide enough cooling power to Axima heat exchanger (4) and cooler (5). M_3 reads the mass flow rate of CO_2 solution (at the beginning of the experiment) and CO_2 hydrate slurry. In the first 2:30 hours, mass flow rate from M_3 was about 0.4 kg/s. When the density and viscosity of the CO_2 hydrate slurry were continuously increasing, see Figure 5.13, mass flow rate of the CO_2 hydrate slurry gradually decreased.

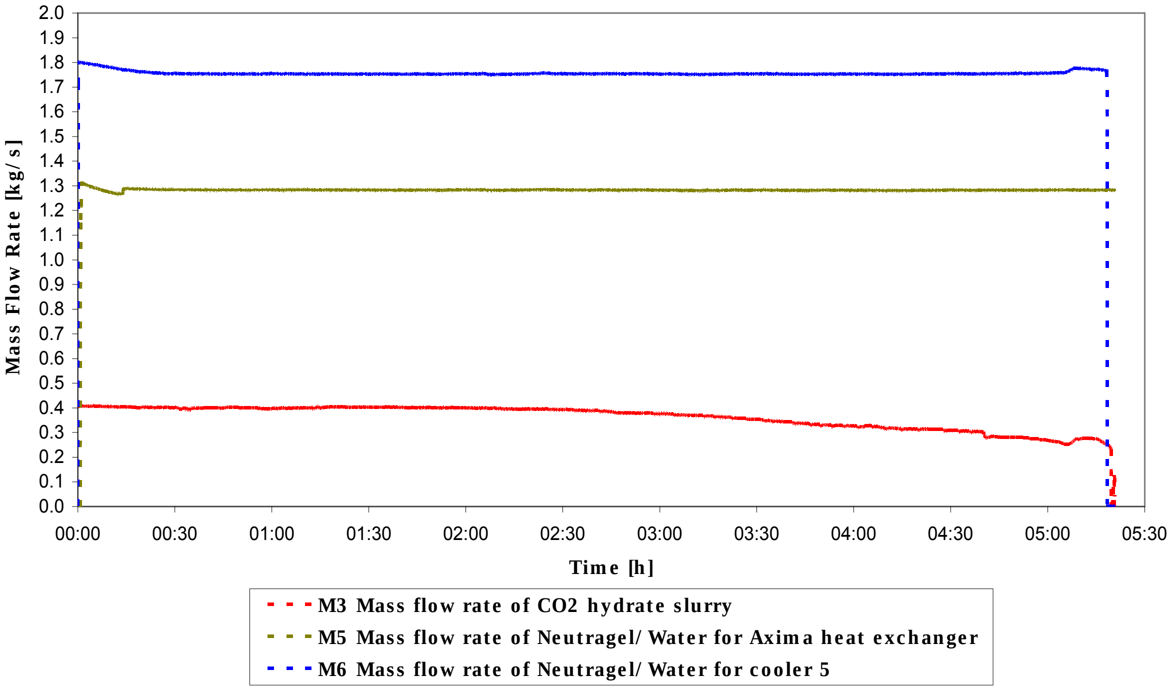

Figure 5.13 Mass Flow Rate of Different Fluids during the Experiment

5.3.3 Pressure in the Loop

The experiment started with a static pressure of 3 bar. The pressure of the closed loop started to increase due to the injection of the CO_2 gas. When the hydrates began to form, huge amount of gas was consumed in the production process. The pressure in the loop drops if injection is stopped. Figure 5.14 shows that the pressure of the loop was controlled between 30 and 35 bar which is a very suitable condition for hydrate production. CO_2 gas was continuously injected when pressure remained within this pressure range. The total amount of gas was obtained from M_1. By the end of the experiment, a total of 3.23 kg of CO_2 gas had been injected.

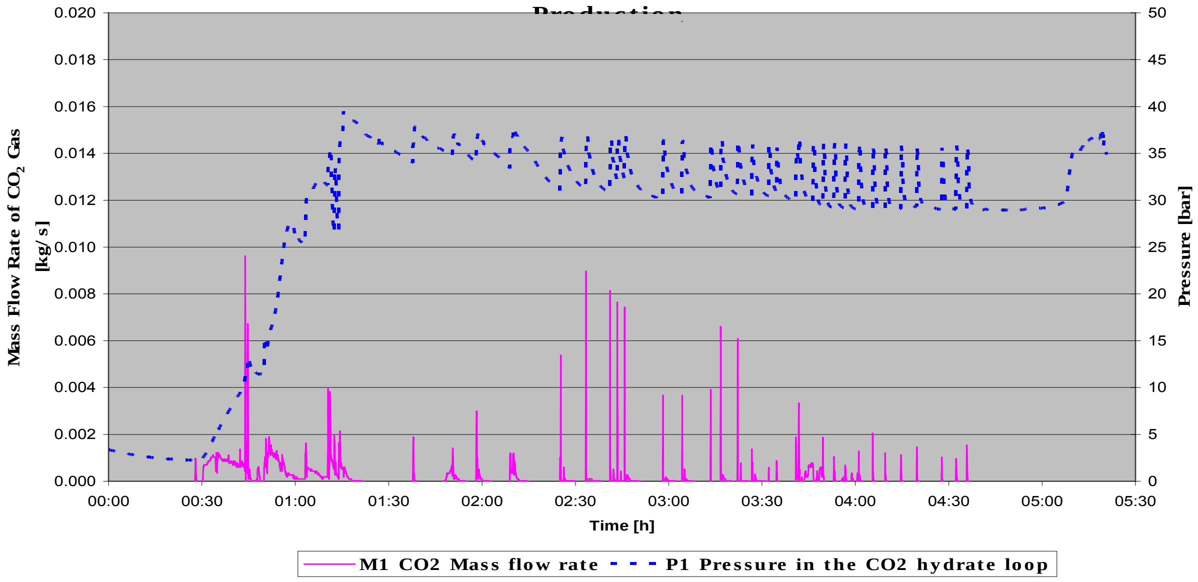

Figure 5.14 Pressure History in the Loop and Mass Flow Rate of Gas

5.3.4 Water and CO_2 Solution Preliminary Density Measurements

Preliminary density measurements for water and CO_2 solution were performed with two Endress+Hauser mass flow meters for temperatures between 0 and 18 °C and pressure between 20 to 30 bar, see Figure 5.15. The CO_2 solution density was found to be 1010 kg/m^3 at 26 bar for a temperature of 11 °C. For the same pressure and temperature conditions, the numerical model provided 1013 kg/m^3.

Theoretical values for the density of water were evaluated as described in Jiawen Hu *et al.* (2007) whilst those of the CO_2 solution were evaluated as reported in Duan, Z. *et al.* (2006).

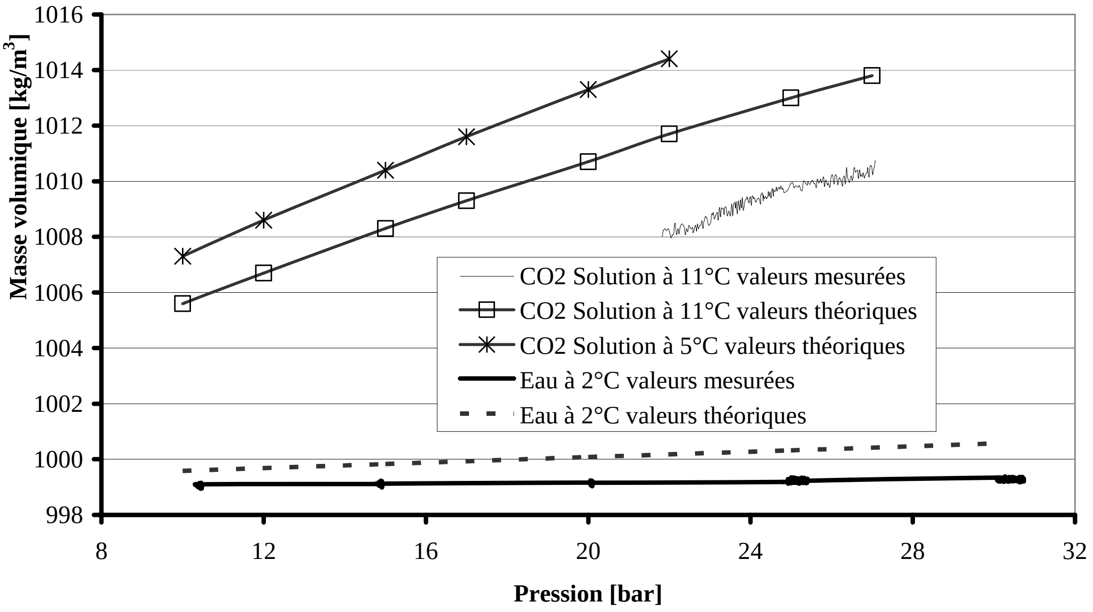

Figure 5.15 Measured and Theoretical Values for the Density of Water and CO_2 Solution

5.3.5 CO_2 Solution and CO_2 Hydrate Density

Figure 5.16 shows the density evolution of the CO_2 solution and the CO_2 hydrate slurry. The value of CO_2 solution density ranged from about 1016 to 1018 kg/m^3. During the experiment, the temperature in the loop was kept between 2 and 3 °C, and the pressure was above 30 bar which are the perfect conditions for hydrate production. CO_2 gas was continuously injected into the hydrate production loop. After 4:30 hours, a density value of 1032 kg/m^3 was reached, which corresponds to over 30% solid fraction. As the viscosity of the hydrate slurry was nearly 5 mPa.s, it seems the high pressure pump was not strong enough to pump the hydrate slurry. Thus, it was decided to stop the gas injection after 4:30 hours.

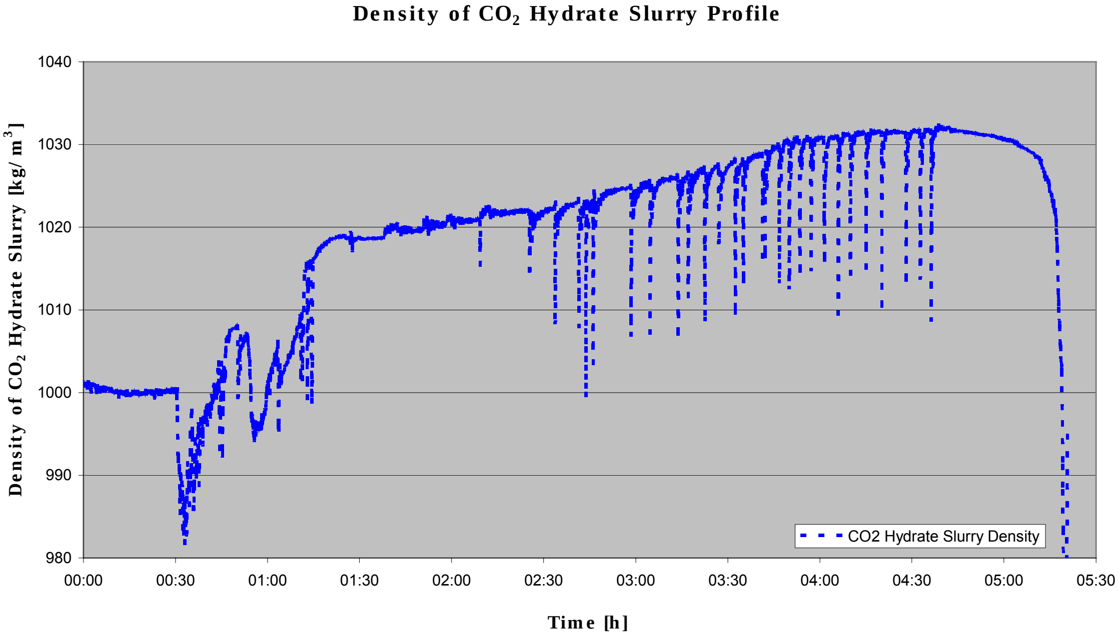

Figure 5.16 Density of CO_2 Solution and Hydrate Slurry

5.4 Micro DSCVII Results

5.4.1 Heat Capacity of Water

Preliminary measurements were performed with the Micro DSCVII to test the accuracy and obtain application notes before measuring enthalpy of the CO_2 hydrate and ice mixture:

1. Heat capacity of water
2. Dissociation enthalpy of ice
3. Heat capacity of ice
4. Determination of freezing point of water in Micro DSCVII
5. Determination of freezing point of water with dissolved CO_2 in Micro DSCVII

Figure 5.17 shows the Cp of water and cited literature value in the region between 2 and 22 °C. Both curves show a similar trend in that when the temperature increases, the Cp value decreases. Literature values are in the range of 4.21 to 4.2 J/kg.K, while the Micro DSCVII measurement values are between 4.28 to 4.25 J/kg.K in the same temperature range. Figure 5.18 shows the average deviation between Micro DSCVII results and literature values. The deviation between the two approaches was only about 1.5% which certifies the DSC results as reliable.

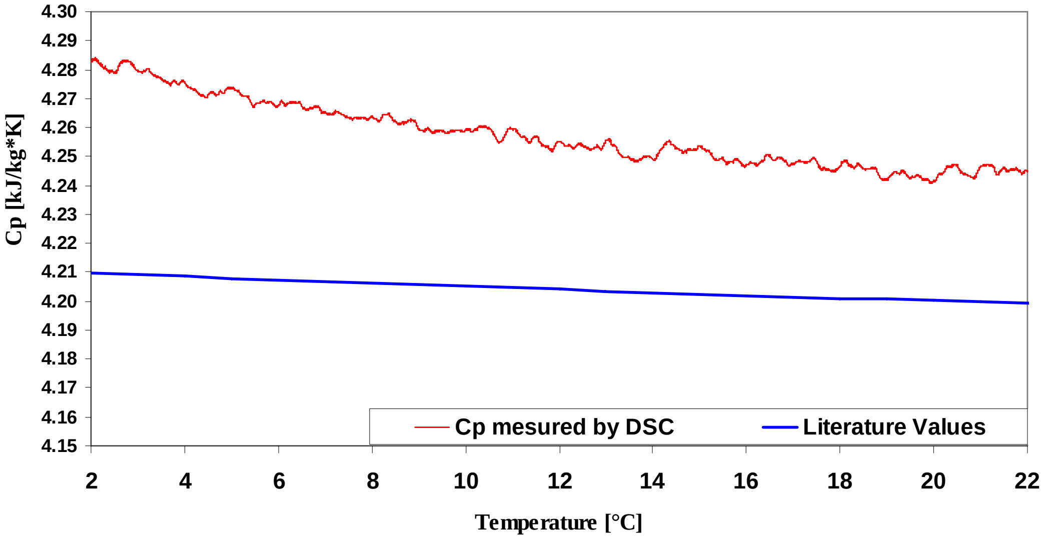

Figure 5.17 Cp of Water Measured by Micro DSCVII between 2 to 22 °C

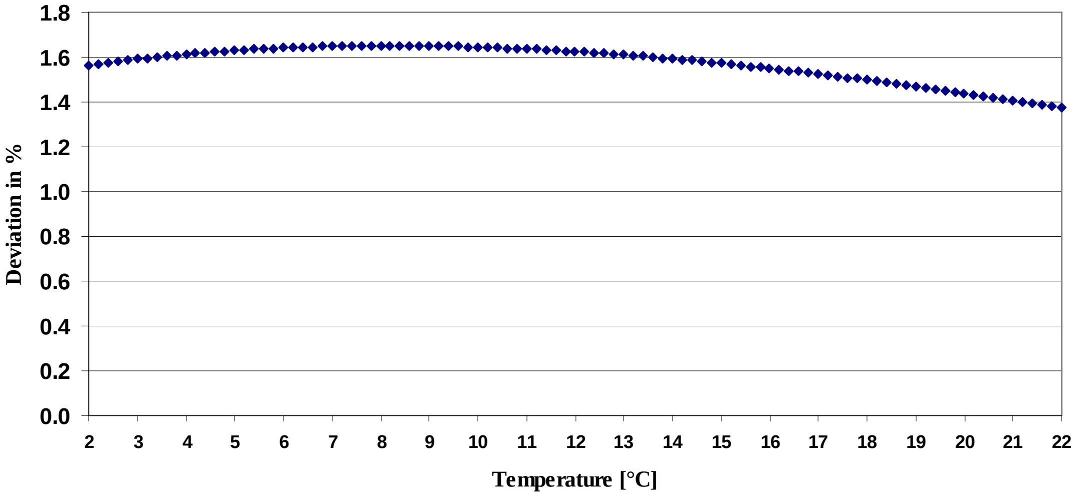

Figure 5.18 Average Deviation between Micro DSCVII and Literature Results

5.4.2 The Dissociation Enthalpy of Ice

The dissociation process of ice, see Figure 5.19, started around -3 °C and completed dissociation around 3 °C in the Micro DSCVII vessel. The enthalpy of dissociation of ice was found to be approximately 334.43 J/g which is in extremely good agreement with the value 333.55 J/g reported by Lide, D.R. (2008).

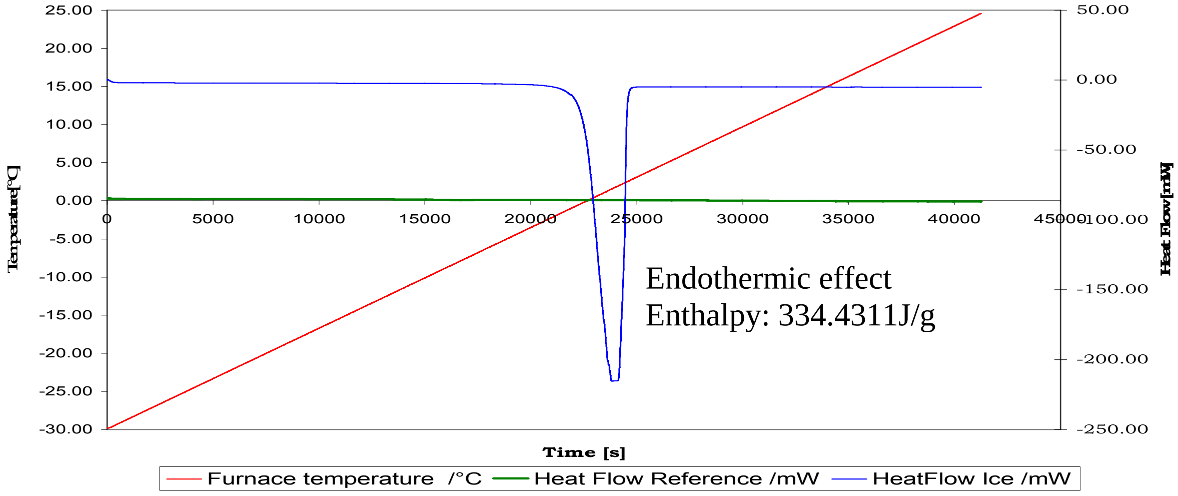

Figure 5.19 Dissociation Enthalpy of Ice Measured by Micro DSCVII (endothermic effect)

5.4.3 Heat Capacity of Ice

Heat capacity of ice was also determined by the Continuous method.

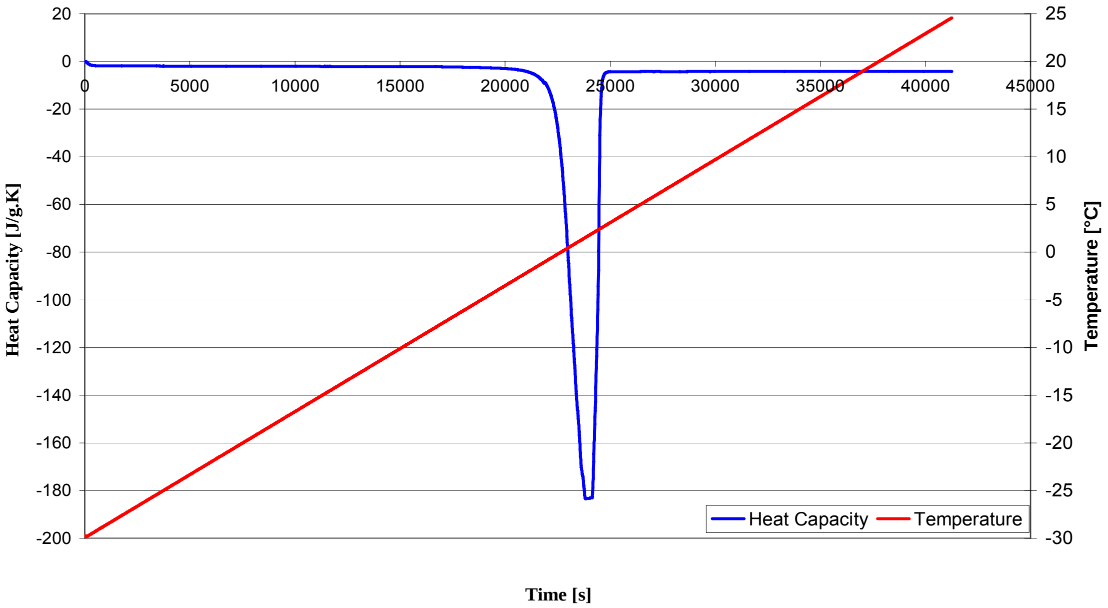

Figure 5.20 Cp of Ice during the Dissociation Process Measured by Micro DSCVII

From Figure 5.20 it can be clearly seen at 1.7 °C, Cp of ice reached the maximum value of 183 J/g.K when ice was undergoing the dissociation process (phase change).

5.4.4 Determination of Freezing Point of Water in Micro DSCVII

At ambient conditions, evaluation of the freezing temperature of tap water is a function of many factors: purity of water, ambient temperature, velocity of airflow around the water, etc. Due to the specific structure of the Micro DSCVII, the freezing point of water in the vessel of the Micro DSCVII can be different from that of water freezing at ambient conditions. Water in the vessel of the Micro DSCVII is not easily frozen since the DSC excludes a number of factors which promote freezing. Thus, it is required to know the freezing point of tap water in order to define the experimental procedure guidelines for hydrate and ice formation processes.

Figure 5.21 shows that tap water began to freeze around -8 °C. The freezing process was over at -9 °C.

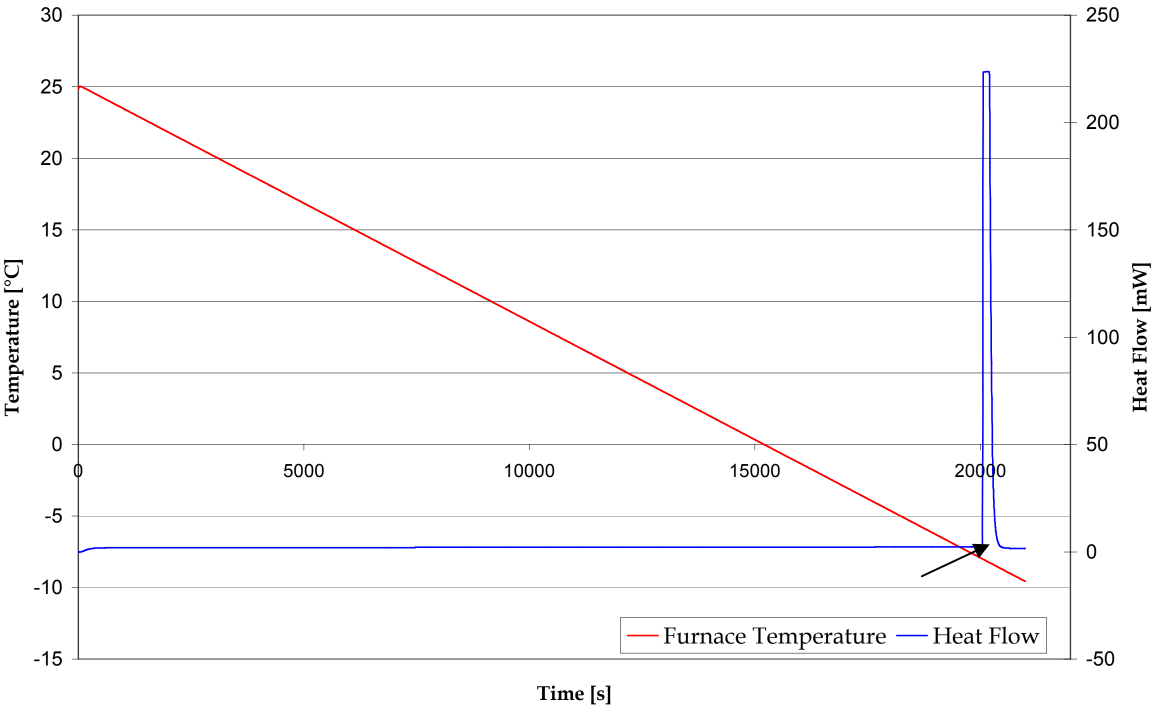

Figure 5.21 Freezing Point of Water Measured by Micro DSCVII

5.4.5 Determination of Freezing Point of Water with Dissolved CO_2 in Micro DSCVII

The freezing point of pure water is 0 °C, but that melting point can be depressed by adding a solvent such as a salt. The use of ordinary salt (sodium chloride, NaCl) on icy roads in the winter helps to melt the ice from the roads by lowering the melting point of the ice. A solution typically has a measuring lower melting point than the pure solvent. This is called freezing point depression in solutions. A more formal treatment of freezing point depression is given by Ebbing, D.D. (1990). The freezing point depression, ΔT_f, is a colligative property of the solution and for dilute solutions is found to be proportional to the molal concentration c_m of the solution:

$$\Delta T_f = K_f c_m \tag{5.1}$$

where K_f is called the freezing-point-depression constant.

The freezing point of the CO_2 solution under 15 bar of CO_2 gas is shown in Figure 5.22. Under 15 bar of CO_2 gas, the gas solubility in water before the water starts to freeze is about 47.615 g/kg_{H_2O}. The mass of tap water sample was taken as 189 mg. About 7 mg of CO_2 gas will dissolve in the water. Hence, the total mass adds to 196 mg.

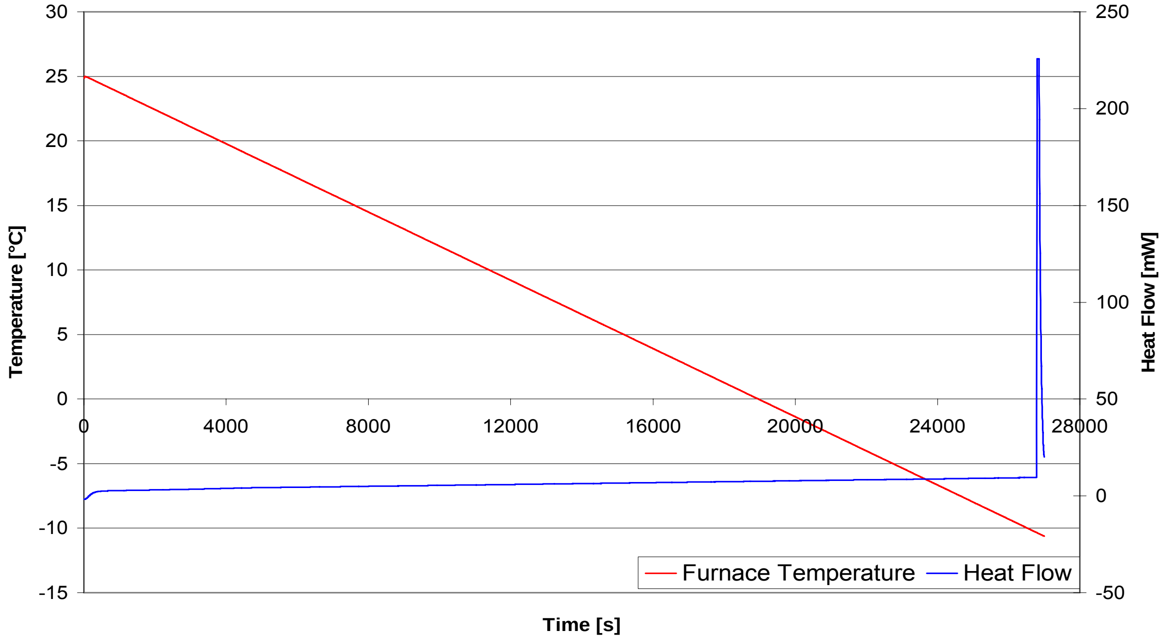

Figure 5.22 The Freezing Point of CO_2 Solution under 15 bar of CO_2 Gas in High Pressure Vessel of Micro DSCVII

From Figure 5.22 it can be seen that the freezing point of water was, as expected, depressed by the dissolved CO_2 gas and formed CO_2 solution. The freeing point of CO_2 solution under 15 bar in the high pressure vessel of Micro DSCVII was around -10.3 °C.

5.4.6 Measurements of CO_2 Hydrate-Ice Mixture

CO_2 Hydrate Formation

Pure CO_2 hydrates are not easy to be obtained inside a DSC. To have pure CO_2 hydrate, the following conditions must be fulfilled: a very expensive high pressure panel with gauge pump needed to guarantee constant formation and dissociation pressure and gas amount; multi-cycle mode of crystallization of CO_2 hydrate must be performed which is rather time consuming and complicated; scanning rate of DSC must be tested to have appropriate cooling speed or heating speed; hydrate formation pressure must be tested to have a proper value to avoid CO_2 gas liquidize prior to form hydrates.

To reduce the complexities, CO_2 hydrate-ice mixture formation and dissociation were performed to obtain the dissociation enthalpy of pure CO_2 hydrate. Based on the described preliminary measurements, a DSC experimental procedure for the CO_2 hydrate-ice mixture was applied. Tap water mass was accurately weighted; a simple pressure panel was adapted to guarantee CO_2 gas pressure around 15 bar during the formation and dissociation process; the Micro DSCVII was cooled down to -15 °C with scanning rate of 0.08 K/min to allow water crystallization and CO_2 hydrate formation; then the Micro DSCVII was heated up to 25 °C at a slow scanning rate of 0.15 K/min. After the ice melting, an endothermic peak linked with CO_2 hydrate dissociation was detected.

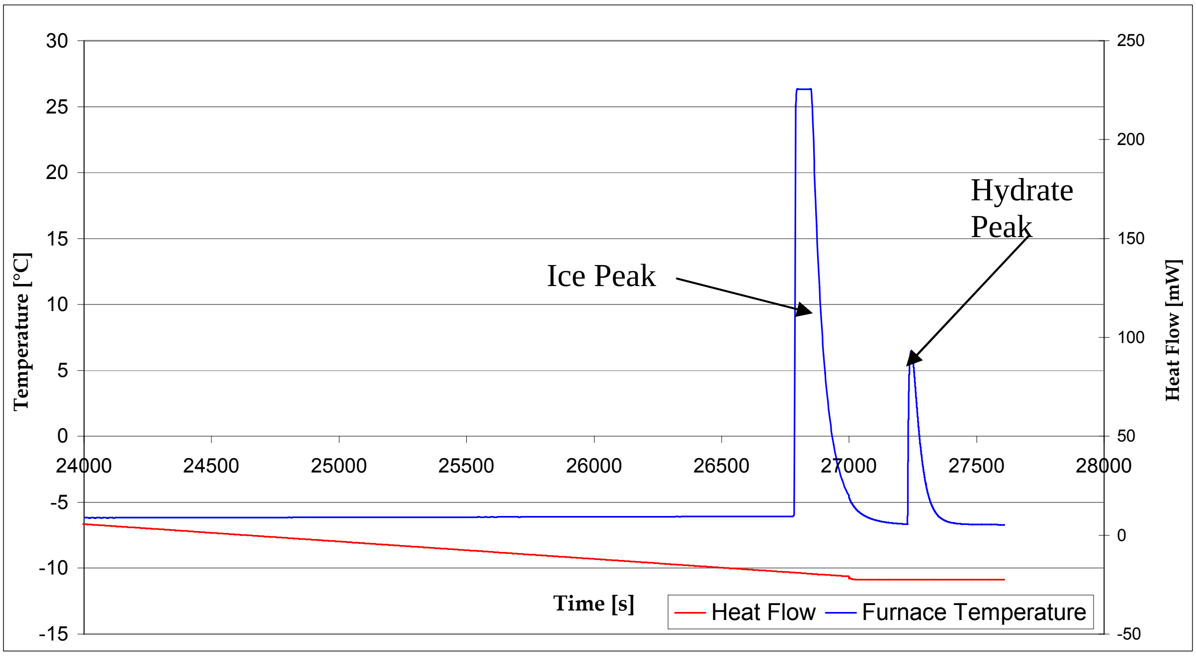

Figure 5.23 The Formation of Ice and CO_2 Hydrate Mixture in the Vessel of the Micro DSCVII under 15 bar

Figure 5.23 shows two exothermic peaks. The first large one corresponds to ice formation while the second one relates to CO_2 hydrate formation. Ice formation occurs prior to hydrate formation. Since ice is easier to form in the DSC, a large portion of water formed ice, released a large amount of heat and only a small portion of water formed CO_2 hydrate. This explains the difference of sizes between the two observed peaks.

CO_2 Hydrate Dissociation

Given the total dissociation enthalpy of the solid formed from CO_2 hydrate-ice mixture, it is possible to estimate the amount of ice and CO_2 hydrate in the mixture. Assuming that all the water present in the vessel is exclusively converted to ice or hydrate, then the following enthalpy balance related to an additive mixture law can be written without taking into account the enthalpy of mixing.

$$\Delta H_{Total} = x^{'}\Delta H_{Ice} + (1 - x^{'})\Delta H_{Hydrate} \qquad (5.2)$$

where ΔH_{Total}, ΔH_{Ice}, $\Delta H_{Hydrate}$ are the total dissociation enthalpy of CO_2 hydrate-ice mixture, the latent heat of pure ice, the dissociation enthalpy of pure hydrate, respectively. $x^{'}$ is the mass fraction of ice, i.e., the mass of formed ice divided by the initial mass of water and (1-$x^{'}$) represents the mass of water contained in the hydrate divided by the initial mass of water.

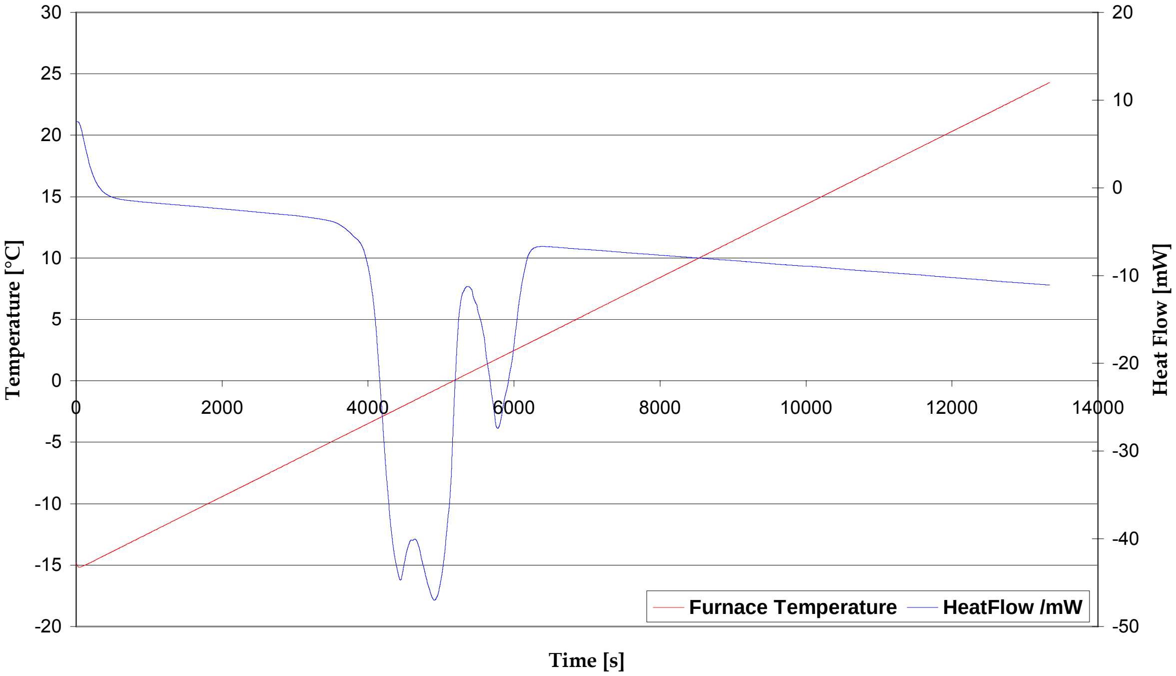

Figure 5.24 The Dissociation of Ice and CO_2 Hydrate Mixture in the Vessel of the Micro DSCVII

Figure 5.24 shows two endothermic peaks. The first large one corresponds to ice dissociation process and the second one relates to CO_2 hydrate dissociation. Ice dissociation occurs prior to hydrate formation. Figure 5.24 also reveals that the mixture is mainly composed of ice since the area (which equals energy) of the first peak is much larger than the one of the second peak.

The total tap water mass was 145.7 mg. Considering the maximum CO_2 gas solubility in the water under 15 bar before crystallization, about 1 mg CO_2 gas dissolved in the water solution. The total mass for the CO_2 hydrate-ice mixture is, therefore, 146.7 mg. By integrating the area of the first peak for the ice formation process, an energy value of 39.64 J is obtained. As ΔH_{Ice} equals 333 J/g, it can be deducted that the ice mass is approximately 119 mg. Ice occupied most mass of CO_2 hydrate-ice mixture. The mass of pure CO_2 hydrate is, then obtained by 146.7 - 119 = 27.7 mg. By integrating the area of the second peak, an energy value of 9.84 J is obtained. Dividing this energy by the mass of pure CO_2 hydrate, gives 355 J/g. Given that the hydrate number, *n*, is approximately 6.2 (i.e. 1 mole of hydrate for every 6.2 mole of water), hydrate dissociation enthalpy is about 55 kJ/mole. The dissociation enthalpy is then 55/6.2 or 8.87 kJ/mole of water. By dividing this dissociation enthalpy by the mole mass of water (0.018 kg/mole), a hydrate enthalpy value of 493 kJ/kg water is achieved which is in very good agreement with the value measured by Sandrine Marinhas *et al.* (2007), who reported a hydrate enthalpy equal to 500 kJ/kg of water.

5.5 Corrosion Measurement

To study the corrosion effects of CO_2 solution as well as CO_2 hydrate slurry on low carbon steel, stainless steel and copper for future air-conditioning industry, a complete cycle (creation and dissociation) of CO_2 hydrate slurry was conducted which included: cooling down the saturated CO_2 solution from room temperature to a temperature around 1 to 2 °C and at a pressure range of 25 to 30 bar; injection of CO_2 gas to reach super saturation conditions; formation and cycling CO_2 hydrate slurry in the loop until the hydrate slurry reaches a temperature of approximately 6 °C; consuming of CO_2 hydrate slurry in the heat exchanger at a temperature above 6 °C until all CO_2 slurry dissociates (around 9 °C).

With the aid of probe tube fittings, the high pressure CS1018 low carbon steel, copper 110 and 304L stainless steel probes were vertically immersed in the CO_2 hydrate slurry transportation pipes. The experiments were conducted at a temperature ranging from 1 to 18 °C and pressure ranging from 25 to 30 bar. High pressure probes were subjected to a complete cycle of CO_2 hydrates slurry formation and dissociation and transferred signals to CMAS analyzer S-50. For stabilisation purposes, CMAS was turned on for more than two hours before monitoring.

A computer was used to collect the data from the CMAS analyzer S-50. Processed signals (such as the maximum localised corrosion current, the maximum cumulative charge, and the average corrosion rate and average cumulative corrosion damage or penetration depth) for each probe were also register in one or more separate data files.

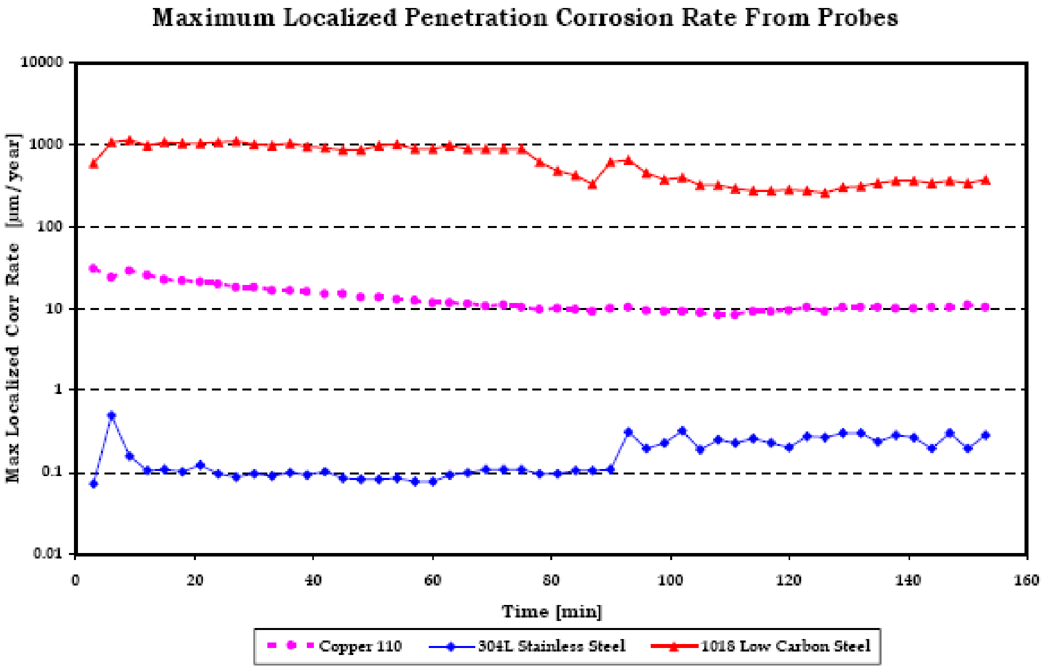

Figure 5.25 : Maximum Localised Corrosion Rates of Different Material Probes during a Short-Term Testing in the CO_2 Hydrate Slurry Loop

The maximum localised penetration rates for type 304L stainless steels were between 0.076 µm/year and 0.5 µm/year. The maximum localised penetration rate for type copper 110 was between 8 µm/year and 30.5 µm/year. The maximum localised penetration rate for type 1018 low carbon steel was between 258 µm/year and 1154 µm/year. The stabilised maximum localised corrosion rates for the three metals varied by nearly 5 orders of magnitude. Short-term experimental results show that type 304L stainless steel displayed very good resistance to the corrosion caused by CO_2 hydrate slurry. Type copper 110 also had good resistance to the corrosion. Type 1018 low carbon steel had very poor resistance to the corrosion.

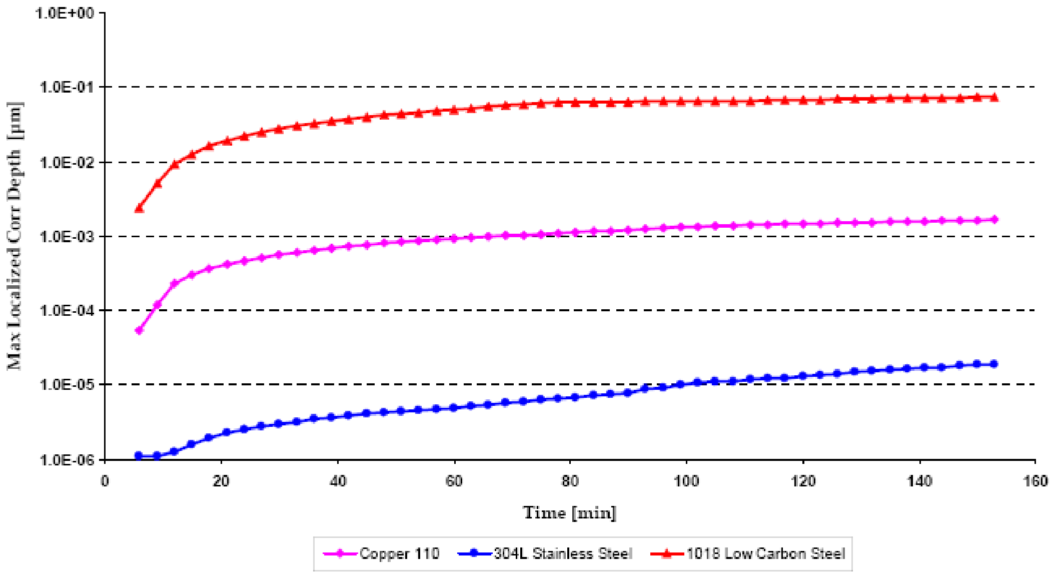

Figure 5.26 Maximum Localised Corrosion Penetration Depth Measured from the Probes

The maximum localised corrosion penetration depths over the testing period were 7.36E-02, 1.65E-03, and 1.89E-05 µm for the electrodes of 1018 low carbon steel probe, copper 110 and 304 L stainless steel probes, respectively. Metal damage on the 304L stainless steel was smallest while on the 1018 low carbon steel was largest.

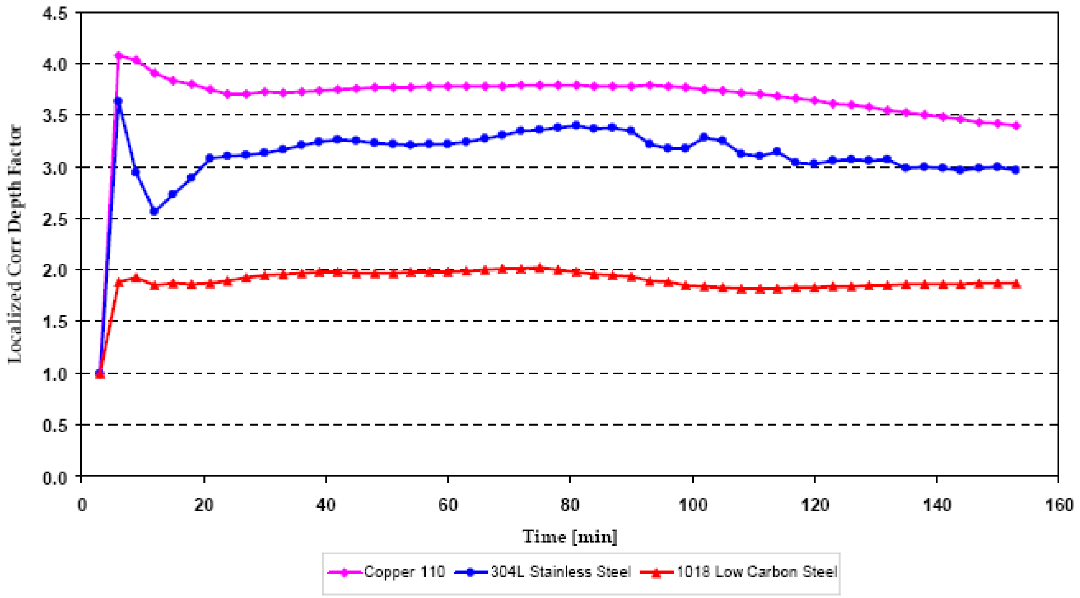

Figure 5.26 Localised Corrosion Depth Factor from Probes

The localised corrosion depth factor shows that the localised corrosion on type 1018 carbon steel was nearly uniform; the localised corrosion on type copper 110 was relatively uniform (not localised); the localised corrosion on type 304L stainless steel was non-uniform even though type 304L stainless steel had extremely low corrosion rate.

During the experiment, several pH tests were carried out and values obtained. The pH value of saturated CO_2 solution as well as CO_2 hydrate slurry was found to be between 5.5 and 6. That means that the CO_2 solution and CO_2 hydrate slurry are both weak acidic substance.

On-line measurement of corrosion rate is feasible and reliable. Even though CO_2 hydrate slurry is a kind of weak acidified substance, it still has negative effects on three test metals when considering the long term usage. This technique may also be applied to investigate the CO_2 hydrate slurry corrosion on other parts of the production system which may use different materials. Experimental results in this report provide important reference data in selecting different materials for the applications of CO_2 hydrate slurry in air conditioning industry, cold storage and other purposes.

6. Conclusions

CO_2 hydrate slurries are a class of non-mechanical generated three-phase secondary refrigerants containing phase change solid particles in suspension in a carrying fluid. These slurries have the advantage of being environmental friendly not only in terms of energy efficiency, thanks to the high latent heat of fusion of the solid phase, but also regarding environmental impact issues. They stand, therefore, as a promising cold carrier for the refrigeration industry. Current worldwide research on the use of these slurries for refrigeration purposes has been, so far, restricted to microscopic scale. In the present report, large-scale continuous CO_2 hydrate formation-dissociation conditions were experimentally investigated on a fully functional laboratory demonstrator for industrial applications. The following conclusions can be drawn:

1- The solid fraction of CO_2 hydrate slurry was evaluated by a numerical approach based on a CO_2 mass balance.

2- A CO_2 hydrate slurry production system with compressor was tested. In this system the CO_2 hydrate slurry formation and dissociation pressure, temperature, density and dynamic viscosity were measured. The density and dynamic viscosity of the CO_2 solution were also measured. The mass flow rates of the different loops composing the system were obtained. The distribution of CO_2 hydrate slurry from the production loop to a climate room was accomplished with success. The consumption of CO_2 hydrate slurry in the consumer installed in the climate room was successful;. The continuous formation and dissociation processes in this loop were not very successful.

2 - A new experimental loop for hydrate production without compressor was completed. The new test rig is an industrial prototype approach. The new test rig is simple, easy to be modified and adapted to new devices. Axima heat exchanger was modified and is being used for hydrate slurry production. Kenics mixing elements and Sulzer SMV gas mixers were tested in the loop. Experimental results showed that the mixing elements and gas mixers can promote hydrate formation. Tap water tests were carried out in the loop to obtain overall energy balances. CO_2 hydrate slurry formation without compressor is feasible; several hours of continuous hydrates formation in the loop was successfully achieved. CO_2 hydrate slurry density was measured with a value of 1032 kg/m^3 which corresponds to over 30% solid fraction (150 kJ/kg dissociation enthalpy of water). Power of the pump was tested and it was showed that it is not sufficient to pump CO_2 hydrate slurry when density is over 1030 kg /m^3; As a result of the lacking power of the pump, the mass flow rate in the test rig was only 0.4 kg/s which degrades the capacity of Axima heat exchanger. As a consequence, Axima heat exchanger was found not to work adequately during the test and energy balances could not be obtained.

3 - The Cp of water and of ice, the enthalpy of ice and of CO_2 hydrates were obtained using a differential scanning calorimetry, Micro DSCVII. Good agreement was observed between the measurements and the values reported in the available literature. In addition, the freezing point of tap water and of the CO_2 solution (this latter under 15 bar) in Micro DSCVII were also measured. It confirmed that CO_2 dissolved in water depresses the freezing point of water. It was also observed that ice formation occurs prior to the CO_2 hydrates formation. In order to obtain more accurate results of the CO_2 hydrate dissociation enthalpy, the total mass of CO_2 hydrate-ice mixture has to be accurately measured. For the moment, the mass of CO_2 dissolved in water is only estimated and this affects the total mass calculation.

Accurate techniques for measuring the CO_2 mass dissolved under high pressure conditions in very small volume of liquid are currently not well developed. Furthermore, better separation and integration of peaks will also provide better results.

4 - On-line measurements of corrosion rates were performed and reliable results obtained. Although CO_2 hydrate slurry is a kind of weak acidified substance, it still has negative effects on the three metals tested when considering the long term usage. This technique may also be applied to investigate CO_2 hydrate slurry corrosion on other parts of the production system which may use different materials. Experimental results in this study provide important reference data in selecting different materials for the applications of CO_2 hydrate slurry in air conditioning industry, cold storage and other purposes.

.

7. Future Work

7.1 New Pump : Optimization of CO_2 Hydrate Slurry Production Loop

Previous experimental results show that when a high density of CO_2 hydrate slurry like 1032 kg/m^3 is reached, the viscosity of hydrate slurry reached almost 4.8 mPa.s and mass flow rate decreases to 0.3 kg/s (from 0.4 kg/s at start).

The power of the high pressure pump (2) is not enough to pump such high density fluid. We will adapt a more powerful high pressure pump or use two pumps in serial to increase capacity; modify two heat exchangers to increase heat transfer coefficient for hydrates formation and dissociation; Optimization of heater (6) to have constant pressure when the heater undergoes the hydrate dissociation process; establish energy balance when hydrates undergo the dissociation process

7.2 New heat exchanger for hydrate slurry production without compressor on the loop

In order to approach industrial prototype, is important to develop a special heat exchanger (evaporator of the cooling machine) with high creation efficiency without compressor on the hydrate slurry loop. With this approach we intend to increase the heat transfer coefficient and global efficiency of the production system.

With this configuration, we use the phase change effect on the two sides (refrigerant of the cooling machine and CO_2 solution) on the evaporator of the cooling machine.

7.3 Determination of Flow Properties of CO_2 Hydrate Slurry

No studies have been reported in the literature regarding viscosity of CO_2 hydrate slurry.

The flow properties of CO_2 hydrate slurry are very important in understanding hydrate formation-dissociation conditions. They stand also as very important reference data when considering hydrate transportation, blockage, etc;

The previous experiments indicate that the Endress+Hauser mass flow meter is not able to predict accurately the viscosity of CO_2 solution and CO_2 hydrate slurry due to the influence of a large amount of accompanying gas bubbles.

Viscosity is a shear measurement. It can only be truly assessed under shear conditions, so it was decided to use shear waves. There are many other types of vibrational waves but these are avoided as they can behave unpredictably in process environments. The XL7-100 viscometer produced by Hydramotion Ltd in UK is a class of instruments called vibrational or resonant viscometers. Vibrational viscometers work by creating waves but it turns out that the type of wave is very important. The solid stainless steel sensor element of XL7-100 is submerged in the fluid and made to move back and forth microscopically at a high frequency. This is called “resonance”. As the surface of the sensor shears through the liquid, energy is lost to the fluid because of its viscosity. The dissipated energy is accurately measured by microprocessor-controlled electronics and then equated back to viscosity. Higher viscosity causes a greater loss of energy and hence a higher reading. The XL7-100 on-line viscometer has been acquired and will be used for the next set of viscosity measurements.

7.2.1 Aims of the Viscosity Measurements

The research aims to evaluate the resonance method for viscosity measurements of CO_2 solutions and CO_2 hydrate slurry and to determine the viscosity dependency on time, temperature, pressure, CO_2 concentration and density.

Experiments are scheduled to begin in January 2008. The following experiments in the loop without static mixing elements and mixer are preview:

- Viscosity of pure water to evaluate the resonance method;
- Viscosity change of CO_2 solution after pressurization of CO_2;
- Viscosity of the CO_2-saturated solution at various temperature, pressure and CO_2 concentration;
- Viscosity of CO_2 hydrate slurry at various temperature, pressure and density;
- Viscosity of CO_2 hydrate slurry undergoing dissociation process;

To improve CO_2 hydrate formation, several static mixing elements and mixer were installed in the pipes of heat exchanger as well as inside the flow pipes of the loop. Static mixing elements and mixer may change the viscosity of CO_2 solution and hydrate slurry. To verify this, the above experiments will be repeated with static mixing elements and mixer in the loop.

Experimental results of water and CO_2 solution will be compared with available literature and conventional experimental method for the determination of the dynamic viscosity by the differential pressure flow meter.

Since these will be the first worldwide results regarding on-line measurement of CO_2 hydrate slurry, these findings are expected to be published in a Journal of Chemical and Engineering data.

7.3 Development of CFD Models to Simulate CO_2 Hydrates Formation/Re-formation Process inside Heat Exchanger

Aims and Objectives:

The overall aim of the modelling work is to develop and test, generalised flow and heat transfer models, based on Computational Fluid Dynamics (CFD) techniques, which can be employed to predict and understand the flow and heat transfer aspects of the formation/re-formation process of CO_2 hydrates inside a heat exchanger. This will involve the following sub-objectives:

- Investigation of applicability of current available, flow and heat transfer models, to simulate the CO_2 hydrates cycle multi-scale interactions.
- Development of comprehensive, efficient and adequate CFD models for the CO_2 hydrates formation/re-formation process inside a heat exchanger.
- Validation of the models using in-situ measurement data.
- Use of the models to perform parametric studies in view of industrial demonstrator.

Research Context and Relevance

Cold production, traditionally by primary refrigerants, accounts for approximately 25% of the total energy consumption in industrialised countries. Growing awareness of the detrimental impact of these synthetic refrigerants on the environment and the general recognition of the need for energy conservation has led to the need to optimise the refrigerating systems performance whilst reducing the refrigerants load at a minimal cost. The most likely area for improvements is the reduction of primary refrigerants by using natural, environmentally friendly secondary refrigerants for cold transport from engine rooms to required areas. In this matter the use of two-phase secondary refrigerants (TPSR) is preferred to a single-phase one because it benefits from high enthalpy due to phase change when slurry melts. Currently, ice slurries are the most used TPSR but the technology is limited by the power of the slurry generator. An alternative is the use of CO_2 hydrates slurry. CO_2 hydrates are crystalline H-bound structures of water with cavities filled by small guest molecules of CO_2. They are generated by injecting CO_2 gas into a cooled liquid phase under specific pressure, temperature conditions. The use of CO_2 hydrate based technologies as a cooling media is not widely spread in industry mainly due to lack of research regarding the slurry formation-dissociation conditions and its physical properties. First studies on the subject have concentrated on the thermal-fluid characterisation of CO_2 hydrate slurry and its suitability for secondary refrigeration applications. More recently, research have been directed towards analyse of the formation-dissociation conditions and the slurry flow characteristics in a small-scale, experimental loop carried out by Marinhas, S. *et al* . (2006). Extension of the technology to industrial scale has been restricted to the works of Sari *et al.* (2007) who have developed a fully functional laboratory demonstrator for industrial applications. Although some modelling work have been performed previously, it has been limited to the field of physical properties so that there is a need for adequate flow and heat transfer models, which can applied in a range of multiphase CO_2 hydrate slurry situations. In particular, there is a great interest to investigate the possibility for formation and re-formation of CO_2 hydrates inside a heat exchanger. An essential step in improving knowledge of the thermal-fluid behaviour of CO_2 hydrate slurries is the development of better methods of prediction such as the ones proposed.

Scope of Work and Methodology

The study implies prediction of the pressure, temperature, density (and in some cases velocity and concentration) distribution inside a heat exchanger tube and comparison with in-situ measurement data. For modelling purposes, the CO_2 hydrates formation/re-formation process inside the heat exchanger can be divided into three stages:

1- Injection of CO_2 gas in water to obtained the aqueous solution.

2- Formation of CO_2 hydrates under specific pressure, temperature and CO_2 concentration conditions.

3- Re-formation of CO_2 hydrates under specific pressure and temperature conditions.

From this, three modelling approaches based on CFD techniques will be defined with building complexity. The study uses a commercial, general-purpose, flow software, FLUENT by ANSYS Inc. (2007) to perform the CFD calculations. The code is based on a finite volume method where all variables such as velocity, temperature, etc are defined at the centre of the control volumes which represent the physical domain.

The proposed work will involve the following steps:

1. Definition of geometry cases, boundary and initial conditions for each stage based on experimental settings.

2. Investigation of the applicability of FLUENT currently available models to adequately simulate each single stage of the hydrates formation/re-formation process. This will be done by investigating the advantages and limitations of the different available Multiphase Models (Eulerian, Mixture and VOF) together with the possibility to couple with other pertinent models such as Phase Change Models and Species Transport and Finite-Rate Chemistry Models.
3. Development of simplified 2-dimensional CFD models for CO_2 formation/re-formation process:

   Stage 1 – To predict pressure rise in a small section of the experimental loop during injection of CO_2, together with gas concentration and overall temperature distribution.

   Stage 2 - To predict, if possible, hydrates formation (exothermic reaction) inside a heat exchanger tube equipped with a static mixing element. In addition, simulation of the overall behaviour of CO_2 hydrates slurry flow.

   Stage 3 - To predict, if possible, hydrates re-formation (exothermic reaction) inside a heat exchanger tube and evaluate re-formation process energy consumption and the possibility of blockage in the system.
4. Development of more complex 3-dimensional CFD models of the stages described above.
5. Validation of CFD models against in-situ measurement data for a range of CO_2 hydrates slurry conditions.
6. Use of validated CFD models to study different CO_2 hydrates slurry conditions and its applicability to industry.

References

[1] ANSYS Fluent Inc., *Fluent 6.3 Documentation*, 2007.

[2] Carroll, J. J., J. D. Slupsky and A. E. Mather, 1991, the solubility of carbon dioxide in water at low pressure, J. Phys. Chem. Ref. Data, 20, # 6, 1201-1209.

[3] Donald E. De Laney, Kevin Tuttle, Brent Baxter, Static Mixers and Melt Transfer Pipes An Introduction, the Extrusion Technicians Toolbox, the Society of Plastics Engineers, June 2004

[4] Duan, Z., N. Møller and J. H. Weare, 1992a, An equation of state for the CH_4-CO_2-H_2O system: I pure systems from 0 to 1000°C and 0 to 8000 bar, Geochim. Cosmochim. Acta, 56, 2605-2617.

[5] Duan, Z and R. Sun, 2003, An improved model calculating CO_2 solubility in pure water and aqueous NaCl solutions from 273 to 533 K and from 0 to 2000 bar, Chem. Geol., 193, 257-271

[6] Duan, Z, Sun R, Zhu C, et al. (2006) An improved model for the calculation of CO_2 solubility in aqueous solutions containing Na^+, K^+, Ca^{2+}, Mg^{2+}, Cl^-, and SO_4^{2-}. Marine Chem., 98 (2-4): 131-139.

[7] Duan, Z, Zhigang Zhang, Equation of state of the H_2O, CO_2, and H_2O–CO_2 systems up to 10 GPa and 2573.15 K: Molecular dynamics simulations with ab initio potential surface, Geochimica et Cosmochimica Acta 70 (2006) 2311–2324

[8] Ebbing, D.D., *General Chemistry*, 3rd Edition, Houghton Mifflin, 1990.

[9] Haar, L., Gallagher, J.S., Kell, G.S., 1984. NBS/NRC Steam Tables: Thermodynamic and Transport Properties and Computer Programs for Vapor and Liquid States of Water in SI Units. Hemisphere Publishing, Washington, DC.

[10] Jiawen Hu , Zhenhao Duan, Chen Zhu , I-Ming Chou, PVTx properties of the CO_2-H_2O and CO_2-H_2O-NaCl systems below 647 K: Assessment of experimental data and thermodynamic models. *Chemical Geology,* 238 (3-4): 249-267, 2007

[11] King, M. B., A. Mubarak, J. D. Kim and T. R. Bott, 1992, The mutual solubilities of water with supercritical and liquid carbon dioxide, J. Supercrit. Fluids, 5, 296-302

[12] Larryn W. Diamond, Nikolay N. Akinfiev, Solubility of CO_2 in water from -1.5°C to 100°C and from 0.1 to 100 MPa: evaluation of literature data and thermodynamic modelling.

[13] Lide, D.R. ed., *CRC Handbook of Chemistry and Physics*, 88th Edition (Internet Version 2008), CRC Press/Taylor and Francis, Boca Raton, FL.

[14] Marinhas, S., Delahaye, A., Fournaison, L., Dalmazzone, D., Furst, W. and Petitet, J.-P, 2006, *Modelling of the available latent heat of a CO_2 hydrate slurry in an experimental loop applied to secondary refrigeration*, Chem. Eng. Process. **45**, pp. 184–192

[15] Marinhas, S., Delahaye, A., Fournaison, L., Martinez, M.C. and Petitet, J.-P, 2006, Etude d'un coulis d'hydrate formé par injection calibre de CO_2 dans un liquid pré-refroidi, Congrès Français de Thermique, SFT 2006, Ile de Ré, France.

[16] Nightswander , J. A., N. Kalogerakis and A. K. Mehrotra, 1989, Solubilities of carbon dioxide in water and 1wt% NaCl solution at pressures up to 10 MPa and temperatures from 80°C to 200°C, J. Chem. Eng. Data, 34, 355-360.

[17] Pitzer, Kenneth S. (1973), "Thermodynamics of Electrolytes. I. Theoretical Basis and General Equations", Journal of Physical Chemistry, Vol. 77, No. 2, January 18, pp. 268-277.

[18] Pitzer, K.S., Peiper, J.C., Busey, R.H., 1984. Thermodynamic properties of aqueous sodium chloride solutions, J. Phys. Chem. Ref.Data 13, 1 – 102.

[19] Portier, S. and C. Rochelle, 2005, Modelling CO_2 solubility in pure water and NaCl-type water from 0 to 300°C and from 1 to 300 bar: applications to Utsira Formation at Sleipner, Chem.Geol. 217, #3-4, 187-199

[20] Rui Sun and Zhenhao Duan, Prediction of CH_4 and CO_2 hydrate phase equilibrium and cage occupancy from ab initio intermolecular potentials Geochimica et Cosmochimica Acta, Volume 69, Issue 18, 15 September 2005, Pages 4411-4424

[21] Sari, O, Hu, J., Brun, F.,Erbeau, N., Homsy, P. and Logel, J.-C, 2007, *In-situ study of the thermal properties of hydrate slurry by high pressure DSC* , 22nd IIR International Congress of Refrigeration, Beijing, China

[22] Wagner W, et al. (2000) The IAPWS Industrial Formulation 1997 for the Thermodynamic Properties of Water and Steam. ASME J. Eng. Gas Turbines and Power, 122: 150-182

[23] Wagner, W., Pruss, A., 2002. The IAPWS formulation 1995 for the thermodynamic properties of ordinary water substance for general and scientific use. J. Phys. Chem. Ref. Data 31 (2), 387–535

[24] Zhang ZG, Duan ZH. (2005) Prediction of the PVT properties of water over wide range of temperatures and pressures from molecular dynamics simulation, Phys. Earth Planetary Interiors, 149 (3-4): 335-354